Invited Papers

Data center links beyond 100 Gbit/s per wavelength

Jose Krause Perin*, Anujit Shastri, Joseph M. Kahn

E. L. Ginzton Laboratory, Department of Electrical Engineering, Stanford University, Stanford, CA 94305, USA

ABSTRACT

Increased traffic demands within and between data centers now necessitate low-cost and low-power systems with per-wavelength bit rates beyond what can be easily achieved using conventional on/off keying. We review spectrally efficient links based on direct detection, Stokes vector detection, coherent detection and differentially coherent detection for data center applications. We show that limited spectral efficiency and power margin will inhibit scaling of direct detection-compatible formats beyond 100 Gbit/s. Stokes vector receivers can provide higher spectral efficiency without requiring a local oscillator laser, but require power-hungry analog-to-digital converters (ADCs) and digital signal processing (DSP). Similarly, existing DSP-based coherent systems designed for long-haul transmission may be excessively complex and power-hungry for short-reach data center links. We present low-power DSP-free coherent and differentially coherent alternatives that avoid high-speed ADCs and DSP and achieve similar performance to their DSP-based counterparts in intra-data center links and dispersion-compensated inter-data center links.

1. Introduction

Global data center internet protocol (IP) traffic is estimated to grow at a compound annual rate of 26.8% from 2015 to 2020, corresponding to a threefold increase in five years [1]. Data center-to-data center IP traffic is expected to grow at an even faster rate of 31.9% [1]. This poses a significant challenge to continuously scaling the capacity of data center links while meeting strict constraints in cost and power consumption, particularly for intra-data center applications, where 77% of the traffic is expected to reside in 2020. User-destined traffic will account for 14% of global data center IP traffic, and the remaining 9% will be between data centers [1].

Scaling the capacity of data center links has long relied on using multiple wavelengths or multiple fibers to carry conventional on-off keying (OOK) signals. This strategy cannot scale much further, however, as 400 Gbit/s links, for instance, would require 16 lanes of 25 Gbit/s, resulting in prohibitively high cost, complexity and power consumption. Recent research has focused on spectrally efficient modulation formats compatible with intensity modulation and direct detection (IM-DD) [2–5] to minimize power consumption. These efforts led to the adoption of four-level pulse amplitude modulation (4-PAM) by the IEEE 802.3bs task force to enable 50 and 100 Gbit/s per wavelength. Nevertheless, 4-PAM systems already face tight optical signal-to-noise ratio (OSNR) and power margin constraints in amplified and unamplified systems, respectively. Moreover, next-generation interconnects will likely need to accommodate increased optical losses due

to fiber plant, wavelength demultiplexing of more channels, and possibly optical switches. To alleviate some of these constraints, both mature and emerging technologies can help on a number of fronts. High-bandwidth, low-power modulators [6] will reduce intersymbol interference (ISI) and improve signal integrity. Segmented modulators [7] may simplify the transmitter-side electronics. Avalanche photodiodes (APD) and semiconductor optical amplifiers (SOA) can improve receiver sensitivity of 100 Gbit/s 4-PAM systems by 4.5 and 6 dB [8], respectively. Improved laser frequency stability, either using athermal lasers [9] or frequency combs [10], will enable dense wavelength-division multiplexing (DWDM) within the data center, possibly yielding a multi-fold increase in capacity.

These technologies will extend the lifetime of 4-PAM, but they do not address the fundamental problem of such IM-DD systems, which is that they only exploit one degree of freedom of optical signals, namely, their intensity. Stokes vector detection has been proposed to enable up to three independent dimensions [11], while avoiding a local oscillator (LO) laser and coherent detection. Nonetheless, Stokes vector receivers rely on power-hungry analog-to-digital converters (ADCs) and digital signal processing (DSP) and do not address the problem of high required OSNR in amplified links or poor receiver sensitivity in unamplified links. Coherent detection allows four degrees of freedom, namely two quadratures in two polarizations, and significantly improve receiver sensitivity due to the LO laser gain. Coherent receivers based on analog signal processing [12] are particularly promising architectures because of their low power consumption, as they avoid high-

speed ADCs and DSP. DSP-based coherent receivers may also become attractive in the future, as demand for even higher spectral efficiency increases, and as those systems are optimized for low-power, short-reach applications by leveraging more advanced complementary metal-oxide semiconductor (CMOS) integrated circuit processes. The high spectral efficiency enabled by coherent detection, combined with its improved receiver sensitivity, will potentially blur distinctions between intra- and inter-data center links.

In this paper, we review and compare these different detection techniques and their enabling technologies. In Section 2, we start by reviewing data center networks and important characteristics of intra- and inter-data center links. In Section 3, we review recent research on modulators, in particular electro-optic Mach-Zehnder modulators (MZMs). In Section 4, we discuss optical fiber requirements. In Section 5, we discuss direct detection (DD)-compatible techniques including M-PAM and orthogonal frequency-division multiplexing (OFDM), also commonly referred to as discrete multitone (DMT). We present comparative results in terms of receiver sensitivity and required OSNR. In Section 6, we review Stokes vector receivers that allow utilization of more than one degree of freedom of the optical channel. In Section 7, we review digital and analog coherent receivers, as well as differentially coherent receivers. In Section 8, we compare the different modulation formats and detection techniques according to their overall complexity and DSP power consumption. In Section 9, we conclude the paper.

2. Data center networks

2.1. Network architectures

In recent years, large internet content providers (ICPs) have begun to host and process large amounts of information in massive, hyperscale data centers. Evolving traffic patterns due to virtualization and cloud computing have led to shifts from north-south traffic, i.e., traffic from outside data centers to servers, to east-west traffic, i.e., traffic from servers to other servers within the same data center or another one nearby.

A traditional data center architecture, as shown in Fig. 1, consists of three tiers. In this scheme, servers connect to access switches that then connect to two aggregation routers for redundancy. These aggregation routers are then connected to core routers with redundancy. While this is an efficient structure to manage north-south traffic, it is inefficient for east-west traffic. Traffic from one server to another in the same data center may travel up to the core layer and then back down, traversing two access switches, two aggregation routers and a core router.

Hyperscale data centers have shifted to a flatter architecture consisting of two tiers [13], as shown in Fig. 2. In this configuration, servers are connected to leaf switches or to top-of-rack (TOR) switches that are connected to leaf switches, which in turn are connected to every spine switch, resulting in a multitude of paths. East-west traffic must
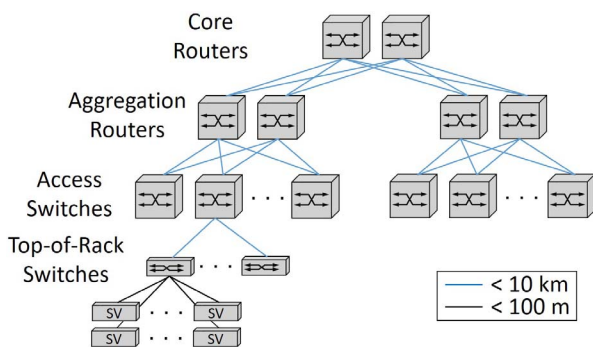

Fig. 1. A traditional three-tier data center architecture. Traffic from one server to another within the data center may need to travel up and through a core router.
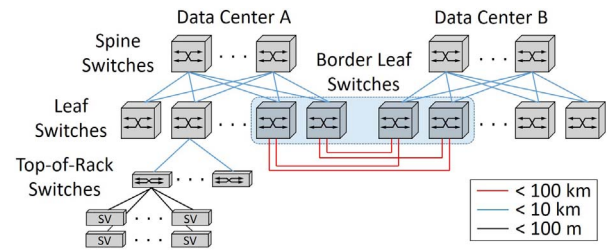

Fig. 2. A newer two-tier data center architecture. Intra-data center links are shown in blue and black, while inter-data center links are shown in red. Every leaf switch is connected to every spine switch. (For interpretation of the references to colour in this figure caption, the reader is referred to the web version of this article.)

now only travel to a spine switch before traveling back down to the desired leaf switch, resulting in low and predictable latency. Expanding the network is readily done by adding more leaf switches or spine switches, as needed. Fault tolerance is also improved, as a single spine switch failing will only result in a marginal decrease in performance. Achieving the full connectivity of the leaf-spine architecture does require more transceivers, as every leaf switch is connected to every spine switch.

Interconnection between nearby (< 100 km) data centers is achieved by interconnecting their border leaf switches, as illustrated in Fig. 2. These inter-data center links have different constraints and impairments than the intra-data center links used within data centers.

2.2. Intra- and inter-data center links

Table 1 summarizes the different constraints and impairments of intra- and inter-data center, in contrast with long-haul systems. In long-haul systems, the high cost and power consumption of complex designs are amortized, as a 3-dB improvement in receiver sensitivity may double the reach and nearly halve the number of required repeaters. Intra- and inter-data center links, however, have other design priorities such as cost, power consumption, and port density, and they face fewer propagation impairments, as polarization mode dispersion (PMD) and nonlinearities are typically negligible over these short propagation distances.

Fig. 3a shows an example system model for an intra-data center link. The transceivers in these links can use multiple wavelengths to achieve high bit rates, but they are typically multiplexed and demultiplexed within the module. Intra-data center links reach up to 10 km and typically operate near 1310 nm to minimize total chromatic dispersion (CD). In this small-CD regime, receiver-side electronic equalization is effective, as shown in the performance curves of Section 5. Moreover, intra-data center links are typically unamplified, resulting in low power margin. APDs and SOAs may improve the receiver sensitivity, as shown in [8] and discussed in Section 5. Current intra-data center links employ either coarse wavelength-division multiplexing (CWDM) with wavelength spacing of 20 nm, or LAN-WDM with wavelength spacing of 4.5 nm to avoid power-hungry laser temperature control. Dense WDM (DWDM) may become commercially viable by leveraging advances in athermal lasers and frequency combs.

Fig. 3b shows an example system model for an inter-data center link. Inter-data center links reach up to 100 km and operate near 1550 nm to leverage erbium-doped fiber amplifiers (EDFAs). CD is significant and must be compensated. As CD is a nonlinear operation in IM-DD systems, simple receiver-side electronic equalization is not effective. Nevertheless, there are other effective electronic CD compensation techniques, which are discussed and compared in Section 5. Alternatively, CD may be compensated optically by dispersion-shifted fibers (DCFs) or tunable fiber Bragg gratings (FBGs) [14], depicted in Fig. 3b by the block CD^{-1}. Though they are less flexible than electronic equalization, they are more power-efficient.

Table 1
Impairments and constraints for intra- and inter-data center links.

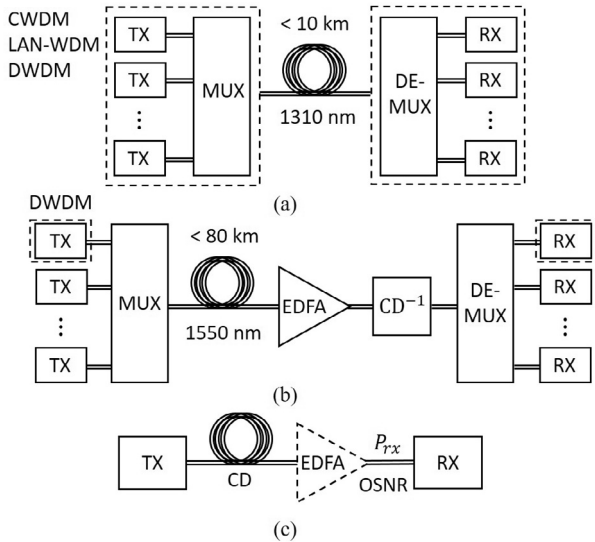| Link Type	Reach (km)	Wavelength (nm)	Wavelength spacing	Main impairments	Amp.	Priorities
Intra-data center	$\leqslant 10$	1310	LAN WDM, CWDM	Pol. rotation	No	Power consumption, power margin, bit rate
Inter-data center	$\leqslant 100$	1550	DWDM	Pol. rotation, CD	Yes	Bit rate, power consumption
Long-haul	$\leqslant 1000$ s	1550	DWDM	PMD, CD, Nonlinearities	Yes	Bit rate, reach

Fig. 3. System-level diagrams of (a) intra-data center links, (b) inter-data center links, and (c) equivalent model for intra- and inter-data center links. The components enclosed in dashed lines in (a) and (b) may be encompassed by a single module. The fiber in (c) corresponds to total dispersion in intra-data center links, and residual dispersion after optical CD compensation in inter-data center links. The optical amplifier in (c) is the equivalent link amplifier, which is omitted when modeling intra-data center links.

Fig. 3c shows the equivalent model used for intra or inter-data center links. In intra-data center links, the fiber represents the total link dispersion and the optical amplifier is omitted. The performance is quantified by computing the receiver sensitivity, which is the received power P_{rx} necessary to achieve a certain target BER, determined by the FEC threshold. For all scenarios, we consider the conventional hard-decision Reed-Solomon code RS(255, 239), which has a net coding gain of 5.6 dB at 10^{-12} BER, an input BER threshold of 1.8×10^{-4} to achieve 10^{-12} BER, and overhead of $\sim 7\%$. Note that the FEC choice is not critical for the performance comparison, since all schemes would benefit from a stronger FEC code.

In inter-data center links, the dispersion corresponds to the residual CD after optical CD compensation. The EDFA corresponds to the equivalent optical amplifier, whose noise figure depends on the number of amplifiers in the link and on their individual noise figures. The performance is quantified in terms of the OSNR necessary to achieve the target BER. The equivalent model of Fig. 3c allows treatment of intra and inter-data center links in the same framework. The difference lies only on whether the link is amplified or not. Hence, the same model could be used for intra-data center links amplified with SOAs. Fiber nonlinearities are not included in the analyses and simulations

presented in the next sections, since data center links are short and operate with relatively small power levels. Polarization effects are only studied for Stokes vector receivers and coherent receivers, discussed in Sections 6 and 7, respectively.

3. Modulators

Although present intra-data center transceivers typically use simple and cost-effective directly modulated lasers (DMLs) or electro-absorption modulators (EAMs), future transceivers will likely shift to MZMs, which are already used in inter-data center transceivers, due to negligible chirp, high bandwidth and the ability to modulate both quadratures of the electric field. In this section, we restrict our focus to MZMs, but DMLs and EAMs are covered in detail in [15,16]. Table 2 shows properties of MZMs implemented in three different materials: lithium niobate (LiNbO3), indium phosphide (InP), and silicon (Si). While LiNbO3 modulators have long been used in long-haul systems, their size makes them unsuitable for the integration necessary for compact, low-power transceivers needed for intra- and inter-data center links. InP and Si, on the other hand, are small and are compatible with high degrees of integration [17,18]. One of the primary drawbacks of Si compared to InP is the lack of a native laser. Si modulators are typically uncooled, owing to the small temperature sensitivity of the free-carrier plasma dispersion effect in Si. From a manufacturing standpoint, Si wafers are much larger and have higher yields than InP wafers. The ability to leverage the mature CMOS process is also a significant advantage for Si, as well as its being an inherently less expensive material. Manufacturing in Si can still be expensive, however, if not done at sufficient scale. High insertion loss is also a potential issue for many Si modulator implementations. Si and InP have their own advantages and disadvantages, but both are viable options for MZMs used in coherent intra- and inter-data center links.

Recent modulator research has focused on heterogeneous integration of other materials on Si as a way to leverage the various advantages of Si while overcoming its shortfalls, notably its potential bandwidth limitations at high symbol rates and its lack of a native laser, as noted above. While InP lasers are commonly used with Si modulators, they are external to the silicon photonic chip, resulting in high alignment costs or high insertion loss. Heterogeneous integration of the InP laser on Si allows for adiabatic coupling from the InP gain region to Si waveguides [19] and, in the future, may lead to lower insertion loss, better integration and cheaper manufacturing. Silicon-organic hybrid modulators are promising candidates for low-power coherent intra- and inter-data center links. By inducing strong electro-optic effects in organic materials placed in the cladding of the modulator waveguide, they offer short modulators with very low drive voltages [6,20]. However, as the induced electro-optic effect can deteriorate within

Table 2
Comparison of electro-optic (EO) modulator material properties. Integration refers to integration with other components.

Material	Native laser	EO effect	$V_\pi L_\pi$ (V·cm)	Insertion loss	Thermal sensitivity	Integration	Comments
LiNbO3	No	Inherent	10	Very low	Very low	No	Discrete components
InP	Yes	Inherent	0.5–1	Low	High	Yes	Small wafers (75 mm)
Si	No	Requires doping	0.2–2	Medium	Very low	Yes	Large wafers (300 mm)
SOH	No	Induced	0.05–0.2	Medium	High	Yes	Uncertain lifespan
Thin-film LiNbO3	No	Inherent	2	Very low	Very low	Yes	

months, further research may be needed to ensure their viability. Integrating LiNbO3 onto silicon can exploit its high-bandwidth electro-optic effect, resulting in wideband modulators [21] that still benefit from silicon's high ability of integration. Thin-film single-crystalline LiNbO3 modulators have been demonstrated with small size, wide bandwidth, and low insertion loss, making them promising candidates for future data center links [22].

Higher-order PAM and quadrature-amplitude modulation (QAM) signals may be generated using segmented MZMs [23,24]. Segmented MZMs preclude the need for digital-to-analog converters (DACs) and linear drivers at the transmitter by allowing binary signaling and limiting drivers to control different segments of the MZM to generate the desired output signal. As segmented MZMs would require several extra segments to support pulse shaping and preemphasis, they are not as desirable for long-haul systems, but could result in significant power and complexity savings for data center links.

4. Optical fiber

The unique requirements of data center links may also motivate reevaluation of optical fiber CD characteristics. When power consumption is the primary concern, fibers with small CD or optical CD compensation should be preferred, since electronic compensation will inevitably be more power-hungry.

As discussed in Section 5, the limited power margin of direct detection links may not support, in the long term, increased optical losses in intra-data center links due to the fiber plant, wavelength demultiplexing of more channels, and possibly optical switches. As a result, it may become convenient to operate intra-data center links near 1550 nm in order to leverage EDFAs. In this scenario, dispersion shifted fibers (DSF) with zero-dispersion wavelength near 1550 nm may be preferred. Note that nonlinear fiber effects, which can be exacerbated by DSF, are negligible in intra-data center links, since they are short (up to a few km) and operate with relatively small power levels due to eye safety constraints. The DSF CD slope near 1550 nm should be small in order to maximize the number of WDM channels supported. Dispersion-flattened optical fibers with zero-dispersion wavelengths near both 1310 nm and 1550 nm bands would allow operability of intra-data center links in both bands.

Amplified inter-data center links would also benefit from small-CD fibers, as these links are limited by the amount of CD that can be compensated electronically or simply tolerated without compensation. As shown in Section 5, at bit rates of 100 Gbit/s, IM-DD systems can compensate for up to 80 ps/nm of dispersion using simple linear equalizers, while DSP-free coherent systems (Section 7) systems can tolerate up to 40 ps/nm without any compensation. As a result, these systems must employ some form of optical CD compensation, either using DCF or tunable FBG. Alternatively, non-zero DSF (NZ-DSF) with 1 or 2 ps/(nm × km) could eliminate the need of optical CD compensation for intermediate-reach inter-data center links, while allowing enough CD to minimize nonlinear effects.

5. Direct detection

This section describes systems based on direct detection of the electric field. This includes M-PAM, OFDM, and single-sideband (SSB) modulation either of single-carrier or multicarrier formats. This section also covers the so-called Kramers-Kronig receiver, which reconstructs the phase of the received electric field from the received intensity waveform.

5.1. Pulse-amplitude modulation

In *M*-PAM, the information is encoded in *M* intensity levels. Fig. 4 shows the block diagram of an *M*-PAM transmitter and receiver. The *M*-PAM transmitter maps the incoming bits onto *M* intensity levels. In the
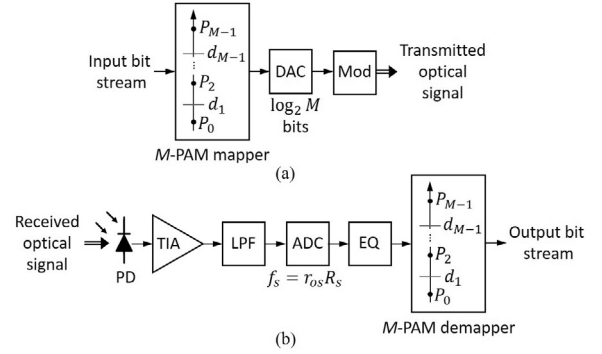

Fig. 4. Block diagram of M-PAM (a) transmitter and (b) receiver.

transmitter in Fig. 4a, the intensity modulator (IM) driving signal is generated by a $\log_2 M$-bit DAC. The transmitter may also realize other operations, such as pulse shaping and pre-equalization or preemphasis, but there are important considerations. Firstly, these operations require higher-resolution DACs, which at high sampling rates (> 50 GS/s) are power-hungry and have narrow bandwidths on the order of 10–15 GHz. Secondly, preemphasis increases the signal peak-to-average power ratio (PAPR). Lastly, after pulse shaping and preemphasis filtering, a relatively large DC bias must be added to make the M-PAM signal non-negative, and thus compatible with intensity modulation. This DC bias directly affects the receiver sensitivity and it was shown to cause a 3-dB power penalty in 100 Gbit/s 4-PAM systems for intra-data center links [2].

In the receiver depicted in Fig. 4b, the optical signal is direct detected, filtered, and converted to the digital domain where adaptive equalization is performed. The equalizer may be a simple feedforward equalizer (FFE) or a decision-feedback equalizer (DFE). Alternatively, the receiver may perform maximum likelihood sequence detection (MLSD). Provided that CD is small, the IM-DD channel is accurately modeled as a linear channel. In this regime, an FFE exhibited only a 1-dB penalty with respect to the optimal and more complex MLSD [2]. For large CD, the fiber IM-DD channel is no longer approximately linear, and FFE or DFE are less effective.

The performance of an *M*-PAM system is determined by the noise variance at each intensity level. There are three scenarios of interest. The first consists of short-reach links in which the receiver uses a positive-intrinsic-negative (PIN) photodiode and thermal noise is dominant. In the next scenario, APD-based receivers have higher sensitivity, but shot noise becomes significant and will affect the noise variance at each level differently. Lastly, in amplified systems with either SOAs or EDFAs, the signal-amplified spontaneous emission (ASE) beat noise is dominant, resulting in different noise variances at the different intensity levels. Although the signal-ASE beat noise is not Gaussian, it can be accurately approximated as Gaussian, as systems with FEC operate at relatively high error rates. For each of these scenarios, we can compute the total noise variance at the kth intensity level:

$$\sigma_k^2 \approx \begin{cases} N_0 \Delta f, & \text{PIN photodiode} \\ N_0 \Delta f + 2qG_{APD}^2 F_A(G_{APD})(RP_k + I_d)\Delta f, & \text{APD} \\ 4G_{AMP}RP_k S_{eq}\Delta f, & \text{optically amplified} \end{cases} \quad (1)$$

where $\Delta f = |H_{rx}(0)H_{eq}(0)|^{-2} \int_0^\infty |H_{rx}(f)H_{eq}(f)|^2 df$ is the receiver one-sided noise bandwidth, where $H_{rx}(f)$ is receiver equivalent frequency response and $H_{eq}(f)$ is the equalizer's equivalent continuous-time frequency response. N_0 is the one-sided thermal noise power spectrum density (PSD) at the receiver, q is the electron charge, G_{APD} is the APD gain, $F_A(G_{APD}) = k_A G_{APD} + (1-k_A)(2-1/G_{APD})$ is the APD excess noise factor, where k_A is the impact ionization factor, which depends only on the material of the APD gain region e.g., $k_A < 0.1$ for Si, and $k_A \approx 0.18$ for InAlAs. R is the photodiode responsivity, I_d is the APD dark current, P_k is the optical power of the kth intensity level at the input of the PIN

photodiode, APD, or the optical amplifier. G_{AMP} is the amplifier gain, and $S_{eq} = \frac{N_A(G_{AMP}-1)F_n\lambda}{2hc}$ is the equivalent one-sided ASE PSD per real dimension [25], where N_A is the number of amplifiers in the link, F_n is the amplifiers noise figure in linear units, λ is the input signal wavelength, h is Planck's constant, and c is the speed of light.

Assuming that all the noises involved are Gaussian distributed and uncorrelated, the BER is given by

$$\mathrm{BER} \approx \frac{1}{M\log_2 M}\left[Q\left(\frac{G_{eff}(d_1-P_0)}{\sigma_0}\right) + \sum_{k=1}^{M-2}\left(Q\left(\frac{G_{eff}(P_k-d_k)}{\sigma_k}\right)\right.\right.$$
$$\left.\left. + Q\left(\frac{G_{eff}(d_{k+1}-P_k)}{\sigma_k}\right)\right) + Q\left(\frac{G_{eff}(P_{M-1}-d_{M-1})}{\sigma_{M-1}}\right)\right] \quad (2)$$

where $Q(\cdot)$ is the well-known Q-function and G_{eff} is the effective gain of the receiver; i.e., $G_{eff} = R$ for unamplified systems; $G_{eff} = RG_{APD}$ for APD-based receivers; and $G_{eff} = RG_{AMP}$ for amplified systems. Eq. (2) assumes that ISI is negligible or was compensated by FFE or DFE. In compensating for ISI, the equalizer causes the well-known phenomenon of noise enhancement, incurring a performance penalty. The effect of noise enhancement is accounted by the receiver noise bandwidth Δf in (1), which would otherwise be $\Delta f = R_s/2$, where R_s is the symbol rate.

The intensity levels $\{P_0,...,P_{M-1}\}$ and the decision thresholds $\{d_1,...,d_{M-1}\}$ are typically equally spaced, but they can be appropriately optimized to minimize the BER. While the exact optimization is intractable, nearly optimal performance is achieved by setting the intensity levels sequentially according to the following heuristics:

$$P_k = P_{k-1} + \frac{Q^{-1}(P_e)}{G_{eff}}(\sigma_k + \sigma_{k-1}) \quad (3)$$

where σ_k^2 is given by (1). Given P_{k-1}, we can determine σ_{k-1}^2 and solve for P_k using (3). Following this procedure, all error events will have equal probability $P_e = \frac{\mathrm{BER}\log_2 M}{2(M-1)}$. This procedure may be realized in an iterative fashion to account for the modulator non-ideal extinction ratio r_{ex}. That is, at the first iteration, $P_0^1 = 0$, and all other levels are calculated according to (3). At the ith iteration, $P_0^{(i)} = r_{ex}P_{M-1}^{(i-1)}$ [8]. We repeat this process until the desired extinction ratio is achieved with reasonable accuracy. Fig. 5 shows optimized intensity levels with their respective conditional probability density functions (PDFs) of the noise. Each error event shown by the shaded areas has equal probability P_e. The decision thresholds are set at the midpoint of the intensity levels. Alternatively, the receiver could sweep the decision thresholds until the BER is minimized. This is equivalent to the point where the conditional PDF of neighboring levels intersect, which corresponds to the maximum
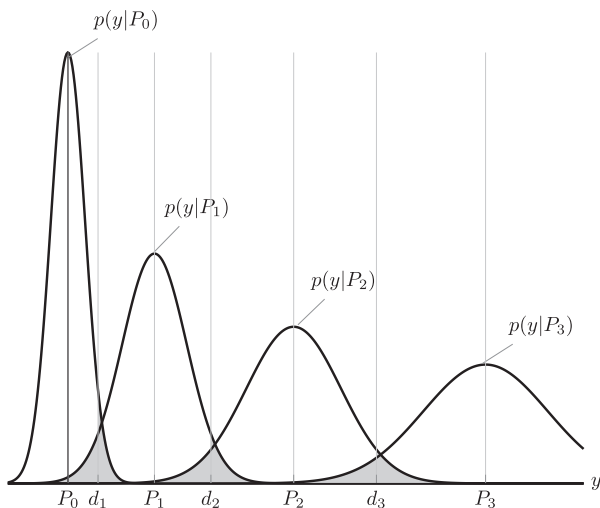

Fig. 5. Example of optimized levels and their corresponding noise conditional probability density functions.

likelihood decision. Even when the noise is not Gaussian, a similar level spacing optimization procedure based on the Karhunen-Love series expansion can be applied to calculate the optimal intensity levels and decision thresholds [8].

For the unamplified systems based on PIN or APD, we characterize the performance in terms of the receiver sensitivity, defined as the average optical power $\overline{P} = 1/M \sum_{k=1}^{M} P_k$ required to achieve the target BER, defined by the FEC threshold. In amplified systems, it is more convenient to characterize the performance in terms of the required OSNR: $\mathrm{OSNR}_{req} = \frac{G_{AMP}\overline{P}}{2S_{eq}B_{ref}}$, where B_{ref} is the reference bandwidth for measuring the OSNR. B_{ref} is typically 0.1 nm, corresponding to $B_{ref} \approx 12.5$ GHz near 1550 nm.

Fig. 6a shows the receiver sensitivity of 4-PAM and other modulation formats vs. dispersion for unamplified systems based either on PIN photodiode or APD. Fig. 6b shows the required OSNR in amplified systems with either an SOA or an EDFA. The other modulation formats are discussed in the following subsections. The dispersion axis may be interpreted as total CD in intra-data center links, or residual CD after optical CD compensation in inter-data center links. The results obtained with the simplified equations presented in this and following subsections are typically within 2 dB of the Monte Carlo simulations. The simulation parameters are summarized in Table 3. 4-PAM outperforms all other candidates in all considered scenarios. The APD-based receiver has nearly 4 dB better sensitivity than the PIN-based receiver. The APD gain is optimized at each point following the procedure in [8], and is approximately $G_{APD} \approx 12$. Level spacing optimization improves the receiver sensitivity by roughly 1 dB for an APD-based receiver (Fig. 6a), while in amplified systems (Fig. 6b), it results in ∼3-dB OSNR improvement.

As observed in Fig. 6, after roughly 50 ps/nm of dispersion, the penalty due to CD increases steeply. This penalty poses a limit in the reach of intra-data center links and restricts the maximum residual dispersion after optical CD compensation in inter-data center links. Several techniques have been proposed to extend the uncompensated reach. Perhaps the most effective is electronic pre-compensation [26,27], whereby the transmitted signal is filtered by the inverse of the fiber frequency response $H_{CD}^{-1}(f) = \exp(0.5j\beta_2(2\pi f)^2 L)$, where $\beta_2 = -(\lambda/2\pi c)D$, D is the dispersion parameter, and λ is the transmission wavelength. In theory, this pre-filtering can compensate any amount of CD, which must be known at the transmitter. The main drawback of this approach is its complexity. In addition to the filters having tens of taps for 100 km, the transmitter requires two DACs and drivers, as well as an in-phase and quadrature (I&Q) modulator.

Vestigial-sideband (VSB) modulation has been proposed to allow uncompensated transmission of 4-PAM over 80 km [28]. In VSB, the intensity-modulated 4-PAM is generated as usual, but the negative sideband is suppressed by an optical filter. The transmitter laser and the optical filter must have fine wavelength stabilization in order to ensure filtering of the correct signal band. SSB modulation has generally better performance than VSB modulation, but as discussed in Section 5.3, comes at the cost of more complex DSP and requires two DACs, two drivers, and an I&Q modulator. Moreover, receiver-side DSP must mitigate the undesirable signal-signal beat interference (SSBI) for either SSB or VSB modulation. SSB modulation and SSBI cancellation are discussed in Section 5.3 for OFDM, but the same considerations apply to single-carrier formats. A detailed comparison of SSB and VSB for OFDM is presented in [29].

Chirp-managed modulators or line coding techniques such as duobinary 4-PAM [30] or Tomlinson-Harashima precoding [31] are less effective, since they do not avoid the power fading due to CD in IM-DD channels. Fig. 7 shows the frequency of the first notch of the IM-DD channel frequency response for several values of transient chirp parameter α. Generally, the first notch cannot fall below half of the symbol rate; otherwise, the noise enhancement penalty becomes exceedingly high. Hence, for 112 Gbit/s 4-PAM, the first notch cannot fall below
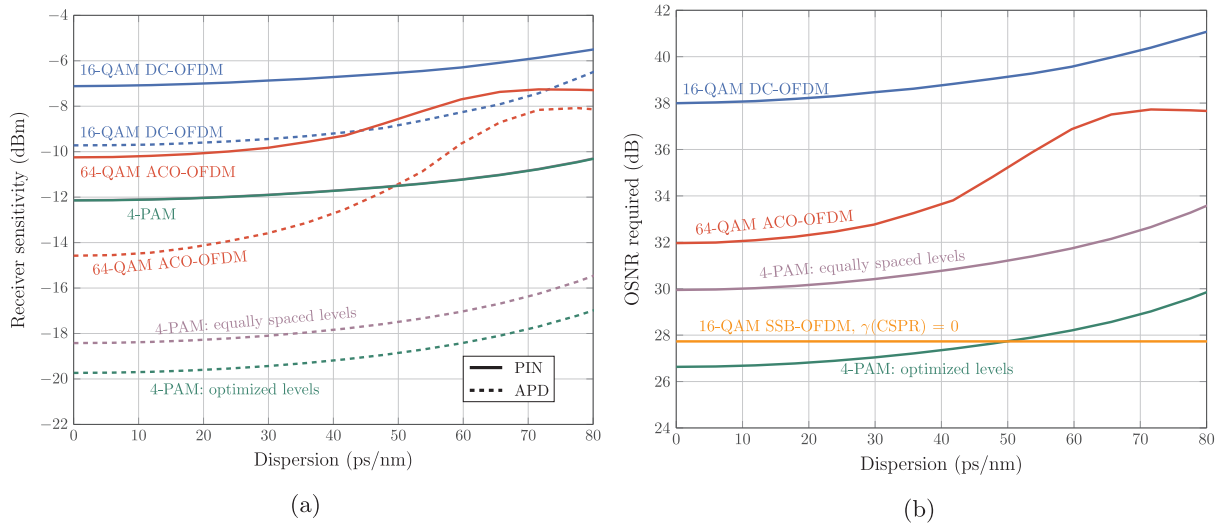
Fig. 6. Comparison of performance of DD-compatible modulation schemes vs chromatic dispersion at 112 Gbit/s. Unamplified systems based on PIN photodiodes or APD are characterized in terms receiver sensitivity 6a, while amplified systems are characterized in terms of OSNR required 6b. The *x*-axis may be interpreted as total dispersion in intra-data center links or residual dispersion after optical CD compensation in inter-data center links (Fig. 3c).

Table 3
Simulation parameters. Monte Carlo simulations used 2^{17} symbols.

Tx	Bit rate (R_b)	112 Gbit/s
	Target BER	1.8×10^{-4}
	Laser linewidth	200 kHz
	Relative intensity noise	-150 dB/Hz
	Modulator bandwidth	30 GHz
	Chirp parameter (α)	0
	Extinction ratio (r_{ex})	-15 dB
PIN & TIA	Responsivity (R)	1 A/W
	Bandwidth	30 GHz
	TIA input-referred noise ($\sqrt{N_0}$)	30 pA/$\sqrt{\text{Hz}}$
APD & TIA [33]	Responsivity (R)	0.74 A/W
	Impact ionization factor (k_A)	0.18
	Gain-Bandwidth product	290 GHz
	Low-gain bandwidth	24 GHz
	TIA input-referred noise ($\sqrt{N_0}$)	30 pA/$\sqrt{\text{Hz}}$
Optical Amplifier	Gain (G_{AMP})	20 dB
	Noise figure (F_n)	5 dB
	Number of amplifiers (N_A)	1
M-PAM Rx	ADC effective resolution	5 bits
	Oversampling rate (r_{os})	5/4
	FFE number of taps (N_{taps})	9
OFDM Rx	ADC effective resolution	5 bits*
	FFT length (N_{FFT})	256
	Oversampling rate (r_{os})	1.23
	Cyclic prefix length (N_{CP})	10

* 6 bits for ACO-OFDM.

Fig. 7. Frequency of first notch of IM-DD channel frequency response for several values of chirp parameter.

5.2. Orthogonal frequency-division multiplexing or discrete multitone

In OFDM, the information is encoded on narrowband and orthogonal subcarriers. In data center literature, OFDM is commonly referred to as DMT, which is terminology borrowed from wireline communications literature, where DMT is often used to describe an OFDM signal transmitted at baseband.

OFDM, in principle, offers higher spectral efficiency than 4-PAM, since the individual subcarriers can be modulated using higher-order QAM. Two variants of OFDM were originally proposed for intensity-modulated data center links: DC-biased OFDM (DC-OFDM) and asymmetrically clipped optical (ACO)-OFDM. These OFDM variants differ in how they meet the non-negativity constraint of the intensity-modulated optical channel, and they achieve different tradeoffs between power efficiency and spectral efficiency. In DC-OFDM, a relatively high DC bias is added to minimize clipping distortion. By contrast, in ACO-OFDM, the entire negative excursion of the signal is clipped, and clipping distortion is avoided by encoding information only on the odd subcarriers [34].

Fig. 8 shows a general block diagram of an OFDM transmitter. A discrete-time OFDM symbol is generated by performing an $N_{FFT} \cdot \text{IFFT}(\cdot)$ operation, where the symbol transmitted on the *n*th subcarrier, Xn is

28 GHz. From Fig. 7, we can see that linear equalization is only effective up to about 100 ps/nm. Chirp increases the first notch frequency, but the maximum dispersion is still below 200 ps/nm. Duobinary 4-PAM encoding and Tomlinson-Harashima precoding narrow the signal bandwidth, but even if the bandwidth is halved, the maximum tolerable dispersion is only on the order of 300 ps/nm. In [32], Tomlinson-Harashima precoding was used in conjunction with DFEs to compensate CD-induced power fading. Tomlinson-Harashima precoding mitigates the error propagation penalty in DFEs, which allows transmission of 56 Gbaud 4-PAM up to 50 km using soft-decision FEC and OSNR required of 38 dB.
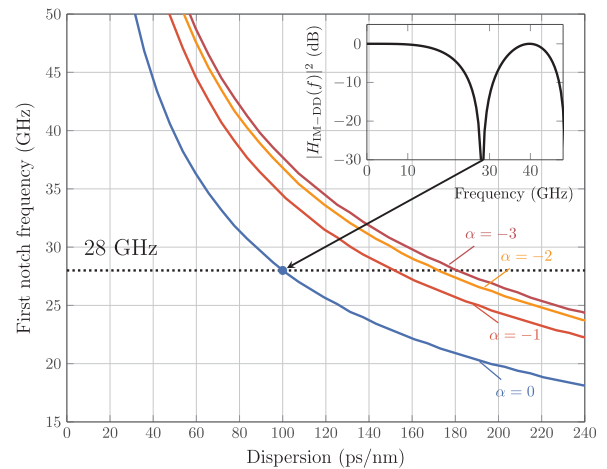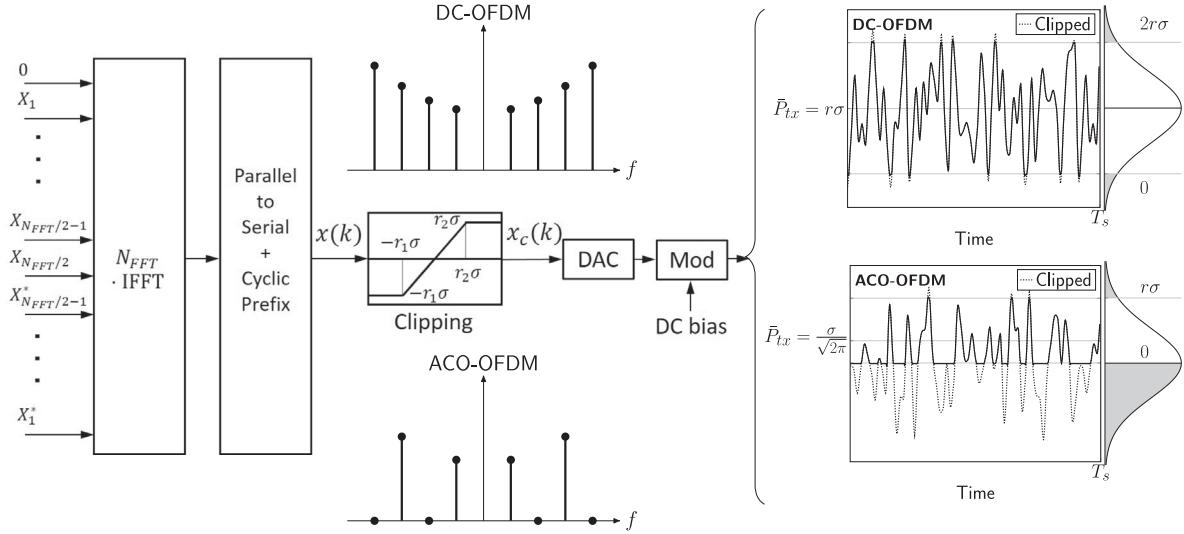
Fig. 8. Block diagram of the OFDM transmitter for DC- and ACO-OFDM. Example time-domain waveforms are shown on the right.

uniformly chosen from a M_n-QAM constellation with average power $P_n = \mathbb{E}(|X_n|^2)$. Hermitian symmetry must be enforced; i.e., $X_n = X_{N-n}^*$, to obtain a real-valued time-domain signal $x[k]$. M_n and P_n are determined from a bit loading and power allocation algorithm. In this paper, we consider the margin-adaptive Levin-Campello algorithm [35], which is the optimal discrete bit loading algorithm for multi-carrier systems with a fixed bit rate.

After parallel-to-serial conversion and cyclic prefix insertion, the discrete-time OFDM signal $x[k]$ is clipped at levels $-r_1\sigma$ and $r_2\sigma$ to reduce the required dynamic range of the DAC and subsequent components. The parameters r_1 and r_2 are referred to as clipping ratios, and σ^2 is the OFDM signal power. Interestingly, by the central limit theorem, for an IFFT length N_{FFT} sufficiently large, the OFDM signal is approximately Gaussian-distributed with zero mean and variance

$$\sigma^2 = 2 \sum_{n=1}^{N_{FFT}/2-1} P_n. \tag{4}$$

In DC-OFDM, the clipping ratio $r_1 = r_2 = r$ determines the tradeoff between clipping distortion and quantization noise. As shown in [3], the optimal choice of the clipping ratio is $r \approx 3$ for a DAC with effective resolution of 5 bits, and $r \approx 3.3$ for a DAC with effective resolution of 6 bits. In ACO-OFDM, $r_1 = 0$ and $r_2 = r$. The distortion caused by clipping the entire negative excursion only falls onto the even subcarriers, which purposely do not carry data [34]. In fact, it can be shown from Bussgang's theorem that $x_c[k] \approx 0.5x[k] + d[k]$, where $x[k]$ and $d[k]$ are uncorrelated, and $d[k]$ only has frequency components at the even subcarriers [34]. Moreover, note that the power of each data-bearing subcarrier drops to $P_n/4$ after clipping.

The clipped OFDM signal is converted to the analog domain by the DAC and an appropriate DC bias is added to make the signal non-negative. Fig. 8 shows example time-domain waveforms of DC-OFDM and ACO-OFDM, which clearly indicate the average-power advantage of ACO-OFDM over DC-OFDM. Formally, the average optical power P_{tx} for each OFDM variant is given by

$$P_{tx} = \begin{cases} r\sigma, & \text{DC-OFDM} \\ \frac{\sigma}{\sqrt{2\pi}}, & \text{ACO-OFDM} \end{cases} \tag{5}$$

The performance of the OFDM signal depends on the received signal-to-noise ratio (SNR) of each data-bearing subcarrier. Assuming that the noises involved are white and consequently equal in all sub-carriers, we can write the noise variance at the nth subcarrier for the same noise scenarios as in Section 5.1:

$$\sigma_n^2 = \begin{cases} f_s \frac{N_0}{2}, & \text{PIN photodiode} \\ f_s\left(\frac{N_0}{2} + qG_{APD}^2 F_A(G_{APD})(R\overline{P}_{rx} + I_d)\right), & \text{APD} \\ f_s(2G_{AMP}R\overline{P}_{rx}S_{eq}), & \text{optically amplified} \end{cases}, \tag{6}$$

where P_{rx} is the average optical power at the receiver input; i.e., the input of the PIN photodiode, the APD, or the optical amplifier. Moreover,

$$f_s = \frac{2pR_b}{\log_2 M} \frac{N_{FFT} + N_{CP}}{N_{FFT}} r_{os} \tag{7}$$

is the sampling rate of the OFDM signal, where $p = 1$ or 2 for DC-OFDM or ACO-OFDM, respectively, accounts for the loss in spectral efficiency by not modulating the even subcarriers. R_b is the bit rate, N_{CP} is the cyclic prefix length and should be larger than the channel memory length, r_{os} is the oversampling ratio of the OFDM signal, and M is the nominal constellation size. After DD, the SNR at the nth subcarrier is given by

$$\text{SNR}_n = \frac{N_{FFT} G_{eff} P_{n,rx}}{\sigma_n^2 + \sigma_Q^2} \tag{8}$$

where $P_{n,rx}$ is the power of the nth subcarrier referred to the receiver input; i.e., to the input of the PIN photodiode, APD, or optical amplifier. Note that a more rigorous analysis would have to account for how signal and noise power are attenuated by the receiver frequency response at each subcarrier. Moreover, quantization noise is no longer negligible and must be included. This formulation assumes that only the receiver quantization noise is significant. As proposed in [36], transmitter-side quantization noise shaping may be performed so that most of the noise energy falls outside the signal band. At the receiver, quantization noise is white and uniformly distributed with variance

$$\sigma_Q^2 \approx \begin{cases} \frac{r^2\sigma_{rx}^2}{3\cdot 2^{2\text{ENOB}}}, & \text{DC-OFDM} \\ \frac{r^2\sigma_{rx}^2}{12\cdot 2^{2\text{ENOB}}}, & \text{ACO-OFDM} \end{cases} \tag{9}$$

where ENOB is the effective number of bits of the ADC, and similarly to (4) $\sigma_{rx}^2 = 2\sum_{n=1}^{N_{FFT}/2-1} G_{eff}^2 P_{n,rx}$ is the OFDM signal variance at the receiver. By the central limit theorem, quantization noise becomes approximately Gaussian distributed after the $1/N_{FFT}\text{FFT}(\cdot)$ operation at the receiver.

The BER is given by the average of the bit error probability in each subcarrier weighted by the number of bits in each subcarrier:

$$\text{BER} = \frac{\sum_{n=1}^{N_{FFT}/2-1} \log_2(M_n) \cdot P_{QAM}(\text{SNR}_n; M_n)}{\sum_{n=1}^{N_{FFT}/2-1} \log_2(M_n)} \tag{10}$$

where $P_{QAM}(\text{SNR}_n; M_n)$ gives the bit error probability for an uncoded M-QAM constellation in an additive white Gaussian noise channel with a given SNR. There are analytical expressions for $P_{QAM}(\text{SNR}_n; M_n)$ for square and non-square QAM constellations [37].

Fig. 6a shows the performance of both DC- and ACO-OFDM in terms of receiver sensitivity vs. dispersion for unamplified systems, and Fig. 6b shows their performance for amplified systems in terms of OSNR required. 4-PAM outperforms both OFDM variants. DC-OFDM has a significant penalty due to the relatively high DC bias required to meet the non-negativity constraint of the intensity-modulated optical channel. Although ACO-OFDM has better performance, it requires prohibitively high DAC/ADC sampling rates (Eq. (7)) due to its low spectral efficiency. In fact, the ACO-OFDM performance curves are not monotonic because, as dispersion increases, subcarriers near the first notch of the IM-DD channel frequency response achieve a poor SNR, so are not used.

Similarly to 4-PAM, CD mitigation through linear equalization is only effective when CD is small. Bit loading and power allocation would allow OFDM variants to better exploit the power-faded optical channel resulting from considerable CD, but such systems are unlikely to be practical, since DD also leads to intermodulation products that fall in the signal band. OFDM can also exploit pre-equalization techniques at the cost of double complexity at the transmitter by using two DACs, two drivers, and an I&Q modulator. More recently, however, SSB-OFDM has been proposed as a viable form of allowing uncompensated transmission for inter-data center links.

5.3. Single-sideband OFDM

In SSB-OFDM, the subcarriers corresponding to the negative sideband are not modulated. The SSB-OFDM signal can still be directly detected, provided that a sufficiently strong unmodulated optical carrier is also transmitted. After DD, the mixing of the unmodulated carrier and the SSB-OFDM signal yields a real-valued double-sideband (DSB)-OFDM signal carrying the same information as the original SSB-OFDM signal. This DSB-OFDM signal does not experience the power fading characteristic of the IM-DD channel. In fact, the DSB-OFDM signal only experiences phase distortion, which can be effectively compensated by electronic equalization.

Fig. 9 shows the block diagram of a SSB-OFDM transmitter. The negative sideband subcarriers are set to zero, and the resulting complex time-domain signal $x[k]$ may be written in terms of a real-valued DSB-OFDM signal $s[k]$:

$$x[k] = x[k] + j\mathscr{H}\{s[k]\}, \tag{11}$$

where $\mathscr{H}\{\cdot\}$ denotes the Hilbert transform.

After clipping, and digital-to-analog conversion, the resulting signals drive an I&Q modulator. The output electric field contains the SSB-OFDM signal $x(t)$ and a carrier component C. The carrier-to-signal power ratio (CSPR), defined as $\text{CSPR} = P_s/P_c = \frac{1}{|C|^2} \sum_{n=1}^{N_{FFT}/2-1} P_n$, characterizes the system performance. The signal propagates through the fiber, whose complex impulse response due to CD is $h_{CD}(t)$. The received signal $y(t)$, after DD is given by

$$y(t) \approx 2RG_{AMP}\sqrt{P_c}\, s(t) * g(t) + 2R\sqrt{G_{AMP}(P_c + P_s)}\, n(t)$$
$$+ RG_{AMP}|x(t) * h_{CD}(t)|^2. \tag{12}$$

The constant terms and the ASE-ASE beat noise were neglected. The operation $*$ denotes linear convolution, $n(t)$ is a white Gaussian noise whose one-sided PSD is S_{eq}, and $g(t)$ is a real-valued impulse response whose Fourier transform is given by [38]

$$G(f) = \begin{cases} H_{CD}(f)e^{-j\varphi_C}, & f > 0 \\ 2\cos\varphi_C, & f = 0 \\ H_{CD}^*(-f)e^{j\varphi_C}, & f < 0 \end{cases} \tag{13}$$

where $\varphi_C = \arg C$, $H_{CD}(f) = \exp(-0.5j\beta_2(2\pi f)^2 L)$. Note that $G(f)$ only causes phase distortion and therefore the desired signal $s(t)$ does not experience power fading. The second term in (12) is the noise component corresponding to the carrier-ASE beat noise and signal-ASE beat noise. The last term in (12) accounts for the SSBI, which is minimized by increasing the CSPR. Nonetheless, the SSB-OFDM receiver must employ some form of SSBI cancellation.

The BER at the nth subcarrier is determined by its corresponding SNR:

$$\text{SNR}_n = \frac{N_{FFT} P_{n,rx} \cdot \text{CSPR}}{(1 + \text{CSPR})\frac{F_n\lambda}{hc}f_s + 2/3r^2 P_s \cdot \text{CSPR} \cdot 2^{-2\text{ENOB}} + \gamma(\text{CSPR})} \tag{14}$$

where $0 \leqslant \gamma(\text{CSPR}) \ll 1$ accounts for imperfect SSI cancellation. $\gamma(\text{CSPR})$ may be interpreted as the remaining power of the SSBI term after SSBI cancellation. This approximation is possible since, by the central limit theorem, any noise after the FFT operation is
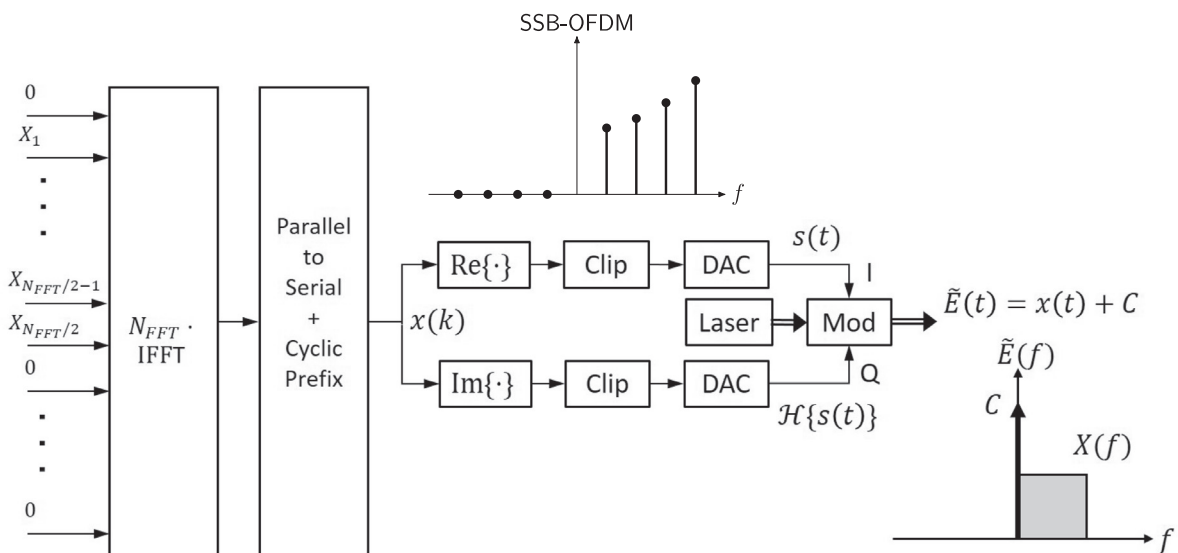

Fig. 9. Block diagram of SSB-OFDM transmitter. Output electric field consists of a SSB-OFDM signal plus a strong unmodulated carrier.

approximately Gaussian distributed. $P_s = \sum_{n=1}^{N_{FFT}/2-1} P_{n,rx}$ is the signal power at the optical amplifier input, where $P_{n,rx}$ is the power of the nth subcarrier referred to the input of the optical amplifier. The three terms in the denominator of SNR_n in (14) account for, respectively, signal-ASE beat noise, quantization noise, and imperfect SSBI cancellation. Knowing the SNR at each subcarrier, we can compute the BER according to (10).

The OSNR required is given by $OSNR_{req} \approx \frac{G_{AMP}P_C}{2S_{sp}B_{ref}}$. In contrast to the DC-OFDM discussed in Section 5.2, the OSNR required no longer depends on the clipping ratio at the transmitter, but it now depends on the carrier power.

Fig. 6b shows the required OSNR for a SSB-OFDM with $\gamma(CSPR) = 0$ (i.e., perfect SSBI cancellation). The required OSNR does not vary with dispersion because, as mentioned above, the detected DSB-OFDM does not experience power fading. The CSPR was optimized for all cases. The ~ 28-dB OSNR required for $\gamma(CSPR) = 0$ is similar to the OSNR required using Kramers-Kronig technique in [39]. For $\gamma(CSPR) = 10^{-7}$, the required OSNR increases to ~ 32 dB and is similar to the OSNR required reported in [39], without SSBI cancellation. These estimated OSNR requirements are, of course, an over-simplification because they assume that the performance difference between the two systems is solely due to the SSBI cancellation technique.

Several SSBI cancellation techniques have been proposed with different efficacies and complexities. In [38], SSBI cancellation is performed by using the received signal $y[k]$ to estimate the SSBI term by computing $|y[k] + j\mathscr{H}\{y[k]\}|^2$ and subtracting it from the received signal. A similar procedure is proposed in [39], where the interference estimate is computed by linearization of the receiver. Due to noise, these techniques are most effective at high OSNR. Moreover, calculating the SSBI estimate in the frequency domain simplifies the Hilbert transform calculation, but it requires frequency-domain convolution to implement the squaring operation. Another technique is based on non-linear equalization based on truncated Volterra series [40]. The number of taps N_{taps} in a Volterra non-linear equalizer grows rapidly, and a simple time-domain implementation has complexity $\mathscr{O}(N_{taps}^2)$. In [40], the Volterra nonlinear equalizer had 28 taps.

Another SSBI cancellation technique proposed in [39] is based on the so-called Kramers-Kronig (KK) receiver [41,42]. In contrast to previous techniques, the KK receiver reconstructs the phase of the electrical field from the detected intensity waveform. This reconstruction is only possible if the electric field signal is minimum phase. As discussed in [41], the minimum-phase condition is guaranteed by transmitting a sufficiently strong carrier. For minimum-phase signals, the phase $\hat{\phi}[k]$ can be estimated from the detected intensity $P[k]$:

$$\hat{\phi}[k] = \mathscr{F}^{-1}\{\mathscr{H}\{\ln\sqrt{P[k]}\}\} = \mathscr{F}^{-1}\{j\text{sgn}(\omega)\mathscr{F}\{\ln\sqrt{P[k]}\}\}, \quad (15)$$

where $\mathscr{F}\{\cdot\}$ and $\mathscr{F}^{-1}\{\cdot\}$ denote direct and inverse discrete-time Fourier transform, respectively. $\text{sgn}(\omega)$ is the sign function and it equals 1, for $\omega > 0; -1$, for $\omega < 0$; and 0, for $\omega = 0$. The electric field $\hat{E}[k]$ can then be reconstructed:

$$\hat{E}[k] = \sqrt{P[k]}e^{j\phi[k]} \quad (16)$$

The reconstructed electric field in (16) corresponds to the SSB-OFDM signal at the receiver, which can be detected as a conventional OFDM signal by removing cyclic prefix, computing the FFT, performing one-tap frequency-domain equalization, and finally performing symbol

detection.

The KK phase retrieval technique outlined in Eq. (15) is not restricted to SSB-OFDM signals. In fact, the KK phase retrieval technique was utilized to reconstruct a SSB 4-PAM signal in [42], and to reconstruct a M-QAM signal in [41]. Note that for QAM, the information on the negative frequency sideband is not redundant. Hence, the transmitted signal must be frequency-shifted by $R_s/2$ with respect to the carrier, where R_s is the signal rate. Consequently, the spectral efficiency of KK M-QAM is halved: $0.5\log_2 M$, which is the same spectrum efficiency achieved by $\sqrt{M}$-PAM modulation. Moreover, this is the same spectral efficiency achieved by carrierless amplitude and phase (CAP) modulation [2] without the SSB requirement and additional complexity of KK phase retrieval. However, CAP does not allow electronic CD compensation. For these reasons, the so-called KK receiver does not improve spectral efficiency or receiver sensitivity.

The KK phase retrieval does permit electronic CD compensation, but at arguably higher DSP complexity than the techniques described previously. The logarithm and square root computations require high-precision arithmetic as well as upsampling by a large factor in order to correctly represent $\ln\sqrt{P[k]}$ in the frequency domain. In [41], an upsampling factor of three was recommended.

6. Stokes vector detection

The DD-compatible modulation formats presented in the previous section have the common drawback that they only exploit one dimension of the optical channel; i.e., optical intensity. Stokes vector detection was proposed to leverage more degrees of freedom of the optical channel while still using DD. In Stokes vector detection, the electric field components $|E_X|^2, |E_Y|^2, \text{Re}\{E_X E_Y^*\}$, and $\text{Im}\{E_X E_Y^*\}$ are detected, and subsequent DSP is realized to recover the transmitted information. This allows up to three independent degrees of freedom of the optical channel; i.e., intensity in X and Y polarizations, and inter-polarization phase. As shown by Morsy-Osman et al. [43], four-dimensional modulation may be achieved by also encoding information on the inter-polarization differential phase, but the receiver has to be significantly modified, increasing the power penalty due to power splitting. Table 4 summarizes recently published experimental results of Stokes vector receivers.

Fig. 10a shows the block diagram of a two-dimensional Stokes vector transmitter, whereby an M-QAM signal is modulated in one of the polarizations, while the other polarization is not modulated. Transmitting an unmodulated carrier allows electronic CD compensation, since similarly to SSB-OFDM, the signal resulting from signal-carrier mixing does not experience power fading. Alternatively, dual-polarization 4-PAM has also been proposed [45], but with smaller tolerance to CD.

Fig. 10b shows the block diagram of a three-dimension Stokes vector transmitter, whereby the intensity of both polarizations are modulated, and the phase difference between two polarizations is also modulated by adding a phase modulator (PM) in one of the polarization branches [11].

Fig. 10c shows the receiver utilized to detect the signals generated by transmitters of Fig. 10a and b. In contrast to a coherent receiver, an LO laser is not necessary, but the Stokes vector receiver still relies on four ADCs and DSP to recover the transmitted information. The cost of

Table 4
Experimental results of various Stokes vector receivers [44].

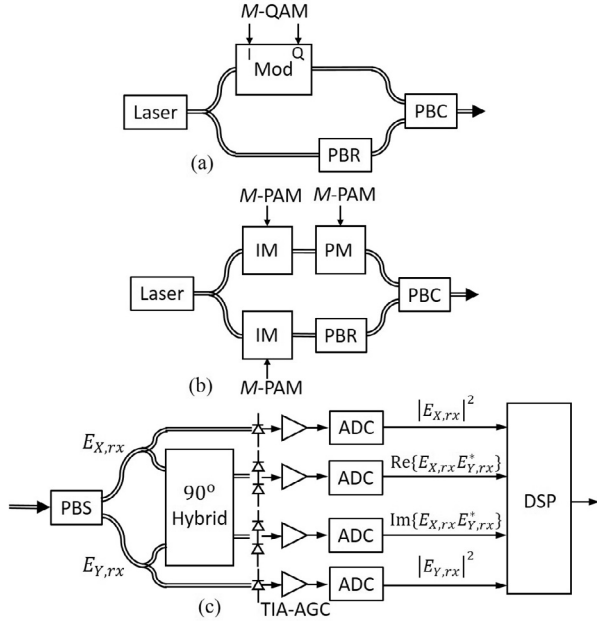| # of dimensions	Modulation	SE (bits/symbol)	Bit rate (Gbit/s)	Reach (km)	Wavelength (nm)	Ref.
2	DP-4-PAM	4	224	10	1310	[45]
2	16-QAM + Carrier	4	224	320	1550	[46]
3	DP-4-PAM + 4-PM	6	300	0	1550	[11]
4	DP-2-PAM + 8-PM + 8-DPM	8	320	10	1550	[43]

Fig. 10. Block diagram of (a) a 2-D transmitter, (b) a 3-D transmitter, and (c) a Stokes vector receiver. Acronyms: polarization beam rotator (PBR), polarization beam combiner (PBC), polarization beam splitter (PBS), intensity modulator (IM), phase modulator (PM), transimpedance amplifier (TIA), automatic gain control (AGC), analog-to-digital converter (ADC), digital signal processor (DSP).

the LO laser and its temperature control to ensure frequency stability required by coherent detection may be amortized by using frequency combs [10]. Moreover, athermal lasers may alleviate the temperate control requirements in coherent systems [9].

The receiver DSP of Fig. 10c is a multiple-input multiple-output (MIMO) equalizer whose function is to compensate for random rotations in polarization as well as mitigate ISI. In Jones space, the electric field in each polarization at the receiver is related to the electric field at the transmitter by a unitary matrix transformation:

$$
\begin{bmatrix} E_{X,rx} \\ E_{Y,rx} \end{bmatrix} = \begin{bmatrix} a & -b \\ b^* & a^* \end{bmatrix} \begin{bmatrix} E_{X,tx} \\ E_{Y,tx} \end{bmatrix}
$$

(17)

where a and b are complex numbers such that $|a|^2 + |b|^2 = 1$.

For the Stokes vector receiver, it is more convenient to write the input and output electric field vectors in a four-dimensional real space:

$$
\begin{bmatrix} |E_{X,rx}|^2 \\ |E_{Y,rx}|^2 \\ \mathrm{Re}\{E_{X,rx}E_{Y,rx}^*\} \\ \mathrm{Im}\{E_{X,rx}E_{Y,rx}^*\} \end{bmatrix}
$$
$$
= \underbrace{\begin{bmatrix} |a|^2 & |b|^2 & -2\mathrm{Re}\{ab^*\} & 2\mathrm{Im}\{ab^*\} \\ |b|^2 & |a|^2 & 2\mathrm{Re}\{ab^*\} & -2\mathrm{Im}\{ab^*\} \\ \mathrm{Re}\{ab\} & -\mathrm{Re}\{ab\} & \mathrm{Re}\{a^2\}-\mathrm{Re}\{b^2\} & -\mathrm{Im}\{a^2\}-\mathrm{Im}\{b^2\} \\ \mathrm{Im}\{ab\} & -\mathrm{Im}\{ab\} & \mathrm{Im}\{a^2\}-\mathrm{Im}\{b^2\} & \mathrm{Re}\{a^2\}+\mathrm{Re}\{b^2\} \end{bmatrix}}_{W}
$$
$$
\begin{bmatrix} |E_{X,tx}|^2 \\ |E_{Y,tx}|^2 \\ \mathrm{Re}\{E_{X,rx}E_{Y,tx}^*\} \\ \mathrm{Im}\{E_{X,rx}E_{Y,tx}^*\} \end{bmatrix},
$$

(18)

where the transfer matrix, defined as W, is not unitary. Note that the entries of the four-dimensional electric field vectors are real and they correspond to the detected signals by the Stokes vector receiver shown in Fig. 10c.

Including noise, the input vector Y to the DSP stage is given by

$$
Y = \begin{bmatrix} |E_{X,rx}|^2 \\ |E_{Y,rx}|^2 \\ \mathrm{Re}\{E_{X,rx}E_{Y,rx}^*\} \\ \mathrm{Im}\{E_{X,rx}E_{Y,rx}^*\} \end{bmatrix} + n,
$$

(19)

where n is a random vector. The covariance matrix of n depends on the receiver noise statistics. In the case of a thermal noise-limited receiver, the covariance matrix is simply $\mathbb{E}(nn^T) = 4\sigma^2 I = 4N_0\Delta f I$. In an amplified system, the noise vector may be approximated by a Gaussian noise vector whose covariance matrix is given by $\mathbb{E}(nn^T) = P_s S_{eq}\Delta f \mathrm{diag}([2,2,1,1])$, where P_s is the received signal total power, assuming equal power in each polarization.

In the ideal case of no ISI, the MIMO equalizer is simply the inverse channel matrix W^{-1}. The resulting decision variables after DSP depend on the number of degrees of freedom used. For instance, in a dual polarization (DP)-4-PAM, only the recovered $|E_X|^2$ and $|E_Y|^2$ are used for decisions, whereas in DP-4-PAM-PM, the entries $\mathrm{Re}\{E_X E_Y^*\}$ and $\mathrm{Im}\{E_X E_Y^*\}$ are used to estimate the inter-polarization phase. Interestingly, since the matrix W is not unitary and neither is W^{-1}, the noise variance in each decision variable is different and, more importantly, it depends on the received polarization state. In fact, in the general case, where the receiver noise has covariance matrix Σ, the output noise covariance matrix is given by $W^{-1}\Sigma W^{-T}$, and the variance in each decision variable is given by the main diagonal entries. As an example, for a thermal-noise limited receiver, the noise variance in the ith decision variable is $4\sigma^2\|W_i^{-1}\|^2$, where W_i^{-1} denotes the ith row of W^{-1}.

Fig. 11a shows box plots for the normalized noise variances; i.e., $\|W_i^{-1}\|^2$, for each decision variable obtained for 10^4 random received states of polarization. The first and second decision variables, corresponding to $|E_X|^2$ and $|E_Y|^2$, are identical and vary from 1 to 1.5, while the third and fourth decision variables, corresponding to $\mathrm{Re}\{E_X E_Y^*\}$ and $\mathrm{Im}\{E_X E_Y^*\}$, are not equal and vary from 0.5 to 1. Hence, the decision variables corresponding to intensity can have twice (3 dB) as much noise as the ones corresponding to phase. Fortunately, as shown in the box plot of Fig. 11b, the OSNR required varies less than 1 dB for random
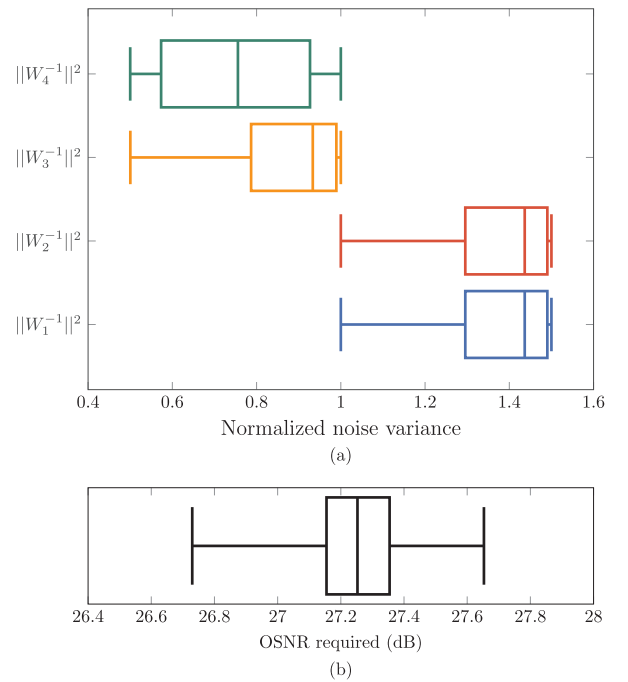

Fig. 11. (a) Box plot of normalized noise variance in each of the decision variables for 10^4 random received states of polarization. (b) Box plot of OSNR required for random received states of polarization for 112 Gbit/s DP-4-PAM 4-PM. The vertical lines denote minimum, first quartile, median, third quartile and maximum, respectively.

states of polarization.

7. Coherent and differentially coherent detection

Coherent and differentially coherent detection offer high spectral efficiency by encoding information in the I and Q quadratures of both polarizations and may provide up to 20 dB improvement in receiver sensitivity by mixing a weak received signal with a strong LO laser. A coherent receiver must perform three basic operations: polarization demultiplexing, carrier recovery, and timing recovery. Differentially coherent detection precludes the need of carrier phase recovery by decoding information encoded in the phase difference between consecutive symbols, but compared to coherent detection it has an inherent SNR penalty, e.g., 2.4 dB for QPSK, and restricts modulation to phase-shift keying (PSK) formats.

We review DSP-based coherent receivers, and how they may be simplified for cost-sensitive data center applications. We show, however, that DSP-free coherent and differentially coherent receivers have substantially smaller power consumption while achieving similar performance to their DSP-based counterparts. As a drawback, it is difficult to scale DSP-free coherent receivers to higher-order (M-ary, $M > 4$) QAM formats, even though the SNR in short-reach links would support these formats.

7.1. DSP-based coherent receiver (DP-M-QAM)

Coherent detection based on high-speed DSP is a mature technology in long-haul systems, but it may be currently unsuitable for data center links, where cost and power consumption are paramount. DSP-based coherent solutions may eventually become viable for short-reach applications by leveraging more power-efficient CMOS processes and optimized implementations for short-reach applications, where fiber impairments are less severe.

Fig. 12 shows a typical implementation of a dual-polarization DSP-based coherent receiver. The incoming signal is split and combined with orthogonal polarizations of the LO laser in two independent 90° hybrids. After balanced photodetection, transimpedance amplifiers (TIAs) with automatic gain control (AGC), and low-pass filtering (LPF) to minimize noise and aliasing, the four outputs are sampled by high-speed ADCs. The DSP stage performs functions such as polarization demultiplexing, PMD compensation, CD compensation, carrier recovery and clock recovery. Some implementations place the DSP chip on the line card itself with an analog interface to the pluggable transceivers, referred to as analog coherent optics (ACO). While this can increase transceiver port density, it essentially offloads the power consumption to elsewhere in the system.

The power consumption of the various operations performed by the receiver was extensively studied in [47]. The most power-hungry operations are CD equalization and polarization demultiplexing with PMD
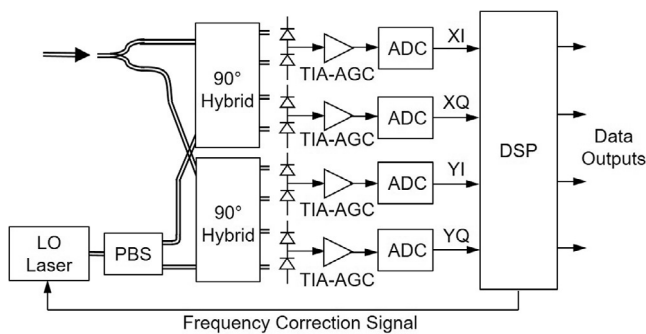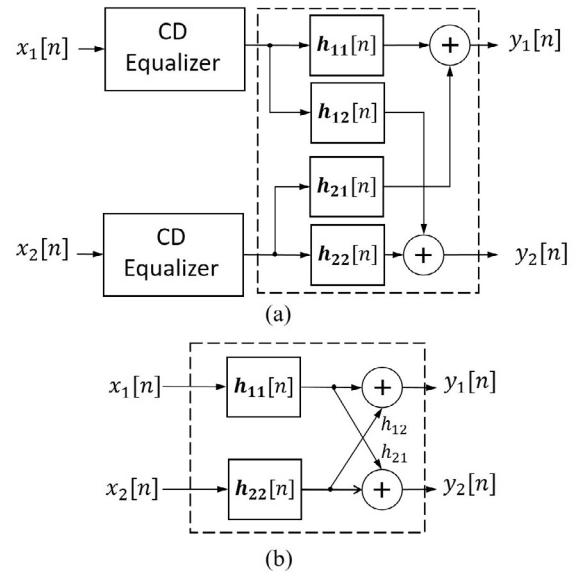

Fig. 13. Block diagram of (a) CD and 2×2 MIMO equalizers used in conventional coherent receivers, and (b) simplified equalizer for short-reach applications assuming small-CD and small-DGD approximation.

compensation, which together amount to roughly 55% of the receiver power consumption [47]. Fig. 13a shows the block diagram of CD equalization and polarization demultiplexing with PMD compensation stages typically used in long-haul systems. First, CD equalization is performed using nearly static frequency-domain equalizers with hundreds of taps. This is followed by a 2×2 MIMO equalizer comprised of filters with typically less than 15 taps that are updated frequently to mitigate PMD and track changes in the received state of polarization.

The CD equalizers may be omitted if CD is small enough such that the filters in the 2×2 MIMO equalizer can compensate for it. Moreover, if the skew between the two polarizations is much smaller than the sampling rate, the coefficients of filter $\boldsymbol{h}_{11}$ are approximately proportional to those of $\boldsymbol{h}_{12}$, and similarly for filters $\boldsymbol{h}_{21}$ and $\boldsymbol{h}_{22}$. Hence, we can simplify the 2×2 MIMO as shown in Fig. 13b, which nearly halves the require number of DSP operations compared to the 2×2 MIMO equalizer in Fig. 13a. The filters $\boldsymbol{h}_{11}$ and $\boldsymbol{h}_{22}$ mitigate ISI caused by CD, PMD, and component bandwidth limitations. The cross terms $\boldsymbol{h}_{12}$ and $\boldsymbol{h}_{21}$ remove the Y component from X and vice versa. Filter coefficient update equations using either least-mean squares (LMS) or constant-modulus amplitude (CMA) algorithms are given in [12, Appendix 2]. This simplification only holds when the mean differential group delay (DGD) between the two polarizations is much smaller than the sampling rate, so that the two polarizations appear synchronized at the receiver. Assuming a sampling rate of 70 GS/s (oversampling ratio of 5/4 at 56 Gbaud), and PMD of 0.1 ps/$\sqrt{\text{km}}$, the small-DGD approximation holds up to ~ 200 km.

To simplify the complexity of the CD equalizers, Martins et al. [48] have proposed a distributive finite-impulse response (FIR) equalizer that leverages the high multiplicity of the quantized FIR filter coefficients to sharply reduce the number of required operations. Compared to a conventional frequency-domain CD equalizer, their distributive FIR equalizer requires 99% fewer multiplications and 30% fewer additions [48].

Assuming that ISI is effectively mitigated and that phase error after carrier recovery is negligible, the BER for square M-QAM signal is approximately

$$\text{BER} \approx \frac{4}{\log_2 M} \frac{\sqrt{M}-1}{\sqrt{M}} Q\left(\sqrt{\frac{3\log_2 M}{M-1}\text{SNR}}\right). \tag{20}$$

In unamplified systems, the receiver noise is dominated by shot-

Fig. 12. Block diagram of a DSP-based coherent receiver. Acronyms: local oscillator (LO), transimpedance amplifier (TIA), automatic gain control (AGC), analog-to-digital converter (ADC), digital signal processor (DSP).
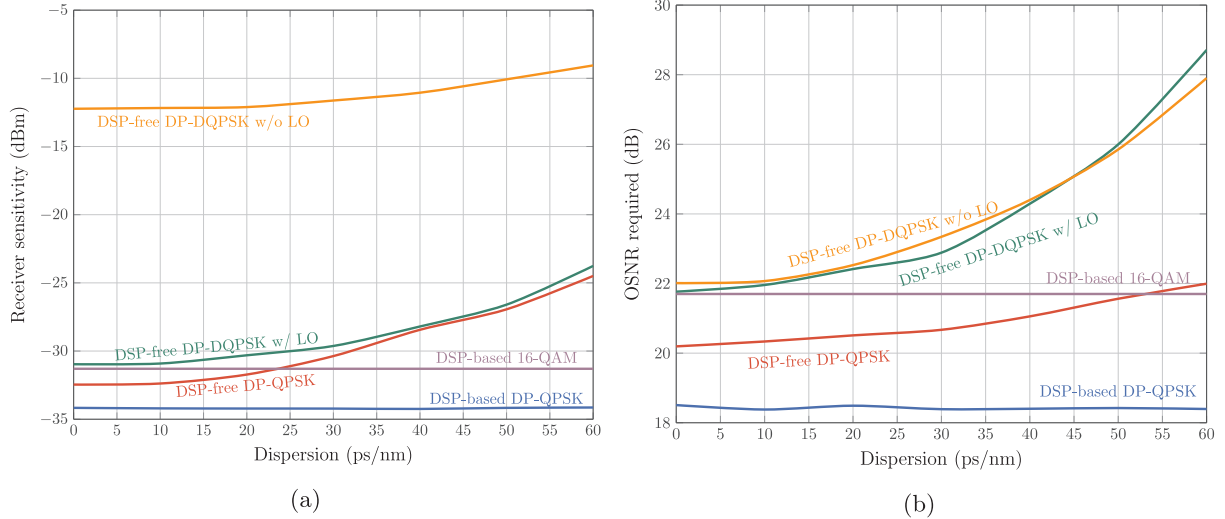
Fig. 14. Comparison of performance of coherent detection schemes vs. dispersion at 224 Gbit/s. Unamplified systems are characterized in terms of (a) receiver sensitivity, while amplified systems are characterized in terms of (b) OSNR required. The x-axis may be interpreted as total dispersion in intra-data center links or residual dispersion after optical CD compensation in inter-data center links (Fig. 3c).

noise due to the strong LO laser signal, while in amplified systems the ASE noise is dominant. The SNR for each of these scenarios is given by

$$
\text{SNR} = \begin{cases} \frac{RP_{rx}}{2q\Delta f}, & \text{shot noise-limited} \\ \frac{RB_{ref}}{\Delta f}, & \text{optically amplified} \end{cases},
\tag{21}
$$

where P_{rx} average received optical power. The receiver noise bandwidth Δf is defined as in (1), and it depends on the receiver LPF and on the equalizer. In DSP-based systems, the combination of anti-alias filtering followed by fractionally spaced adaptive equalization achieves similar performance to the optimal receiver consisting of analog matched filtering and symbol-rate equalizer. In this case, $\Delta f \approx R_s/2$. The difference between Δf and $R_s/2$ corresponds to the noise enhancement penalty. For DSP-free receivers, discussed in the following subsection, the noise bandwidth is determined solely by the receiver LPF.

Fig. 14 shows the performance of various coherent and differentially coherent systems as a function of dispersion (or residual dispersion after optical dispersion compensation). The simulation parameters are shown in Table 5. The curves in Fig. 14 for DSP-based receivers are flat across dispersion values, as CD is effectively compensated by electronic equalization. DSP-based coherent detection systems can use higher-order modulation, such as 16-QAM, to reduce the bandwidth required of electro-optic components. For intra-data center links or inter-data center links with optical dispersion compensation, DSP-free solutions can significantly reduce power consumption. The other curves in Fig. 14 are discussed in the following subsections.

7.2. DSP-free coherent receiver (DP-QPSK)

Coherent detection using analog signal processing was studied extensively in the 1980s and early 1990s [49], but the advent of the EDFA and later DSP-based coherent detection diminished its popularity.

Fig. 15 shows the proposed implementation of a DSP-free coherent receiver [12]. Polarization demultiplexing is performed by optical phase shifters that are controlled by low-speed circuitry. Other receiver operations such as carrier recovery, timing recovery and detection are performed in the high-speed analog electronics stage. Timing recovery and detection may be realized using conventional clock and data recovery (CDR) techniques [50]; thus, we do not discuss them further herein.

The polarization controller, shown by the inset in Fig. 15, must recover the transmitted state of polarization by inverting the fiber

Table 5

Coherent and differentially coherent systems simulation parameters. Monte Carlo simulations used 2^{17} symbols.

Tx	Bit rate (R_b)	224 Gbit/s
	Target BER	1.8×10^{-4}
	Laser linewidth	200 kHz
	Relative intensity noise	-150 dB/Hz
	Modulator bandwidth	30 GHz
	Chirp parameter (α)	0
	Extinction ratio (r_{ex})	-15 dB
Rx	Photodiode responsivity (R)	1 A/W
	TIA input-referred noise ($\sqrt{N_0}$)	30 pA/$\sqrt{\text{Hz}}$
Optical Amplifier	Gain (G_{AMP})	20 dB*
	Noise figure (F_n)	5 dB
	Number of amplifiers (N_A)	1
LO Laser	Linewidth	200 kHz
	Output power	15 dBm
	Relative intensity noise	-150 dB/Hz
DSP	ADC effective resolution	4 bits
	Oversampling rate (r_{os})	5/4
	Equalizer number of taps (N_{taps})	7
	Filter adaptation algorithm	CMA
Analog Carrier Recovery	Loop filter damping factor (ξ)	$\sqrt{2}/2$
	Loop delay (τ_d)	213 ps
	Optimal natural frequency (f_*)	123 MHz

* 30 dB for LO-free DP-DQPSK.

polarization transfer matrix. Three cascaded phase shifter pairs can perform any arbitrary polarization rotation [51]. The unitary matrix describing polarization rotation caused by fiber propagation in the absence of polarization-dependent loss (PDL) and PMD can be written as:

$$
T_{fiber} = \begin{bmatrix} e^{j\alpha_1} & 0 \\ 0 & e^{-j\alpha_1} \end{bmatrix} \begin{bmatrix} \cos(\zeta) & -j\sin(\zeta) \\ -j\sin(\zeta) & \cos(\zeta) \end{bmatrix} \begin{bmatrix} e^{j\alpha_0} & 0 \\ 0 & e^{-j\alpha_0} \end{bmatrix},
\tag{22}
$$

where α_0, ζ, and α_1 are random, time-varying rotation variables that describe polarization rotation through the fiber. To compensate for the fiber's polarization transformation matrix, a similar matrix can be obtained by the polarization controller:

$$
T_{controller} = \begin{bmatrix} e^{j\phi_1} & 0 \\ 0 & e^{-j\phi_1} \end{bmatrix} \begin{bmatrix} \cos(\theta) & -j\sin(\theta) \\ -j\sin(\theta) & \cos(\theta) \end{bmatrix} \begin{bmatrix} e^{j\phi_0} & 0 \\ 0 & e^{-j\phi_0} \end{bmatrix},
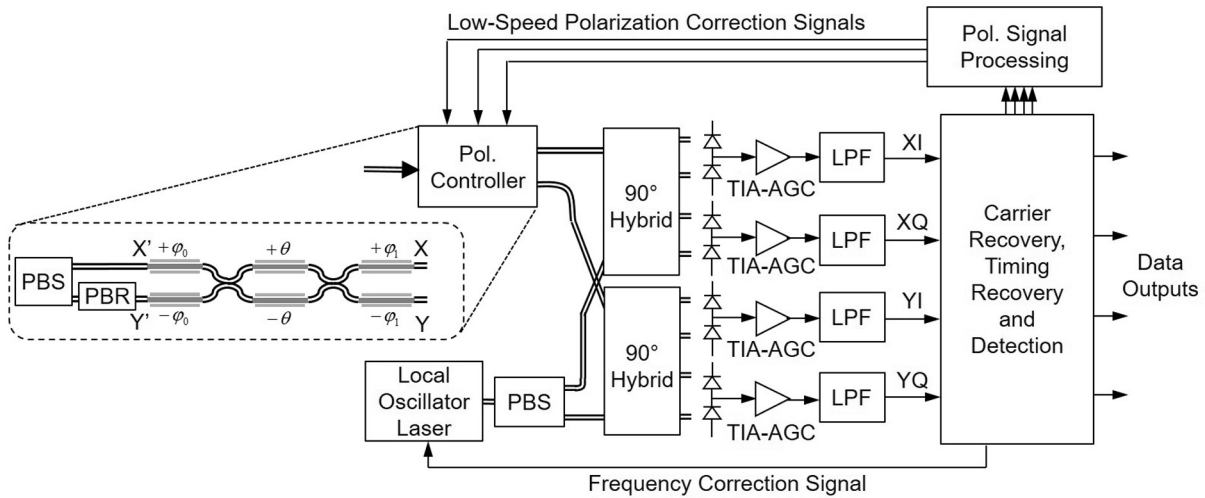\tag{23}
$$

Fig. 15. Block diagram of coherent receiver architectures based on analog signal processing. Acronyms: local oscillator (LO), polarization beam splitter (PBS), polarization beam rotator (PBR), transimpedance amplifier (TIA), automatic gain control (AGC), analog-to-digital converter (ADC), low-pass filter (LPF).

where ϕ_0, θ, and ϕ_1 correspond to the amounts of differential phase shifts in the phase shifters shown by the inset in Fig. 15. One way to control these variables is to transmit a marker tone in one quadrature of one polarization and minimize its presence in the other quadrature and polarization at the receiver. We have demonstrated compensation of up to 700 rad/s of polarization rotation in Monte Carlo simulations [12]. Faster tracking speeds can be obtained with larger changes of angles in the phase shifters, resulting in slightly higher average polarization compensation error, a tradeoff that must be optimized. This method can be used for QPSK, as well as for 16-QAM and higher-order formats. Implementation of the phase shifters can be done using silica, LiNbO3 or any other material that has low loss and allows integration of a sequence of phase shifters. The phase shifters and waveguides do not need to necessarily support two polarizations, as the demultiplexing is performed through phase shifts and coupling, not birefringence. Endless polarization control can be achieved by cascading more phase shifting sections or using a material such as LiNbO3 for phase shifters and resetting them fast enough to allow interleaving and FEC to correct the burst errors. As polarization rotation through a fiber is a relatively slow (milliseconds), time-varying effect [52], the polarization signal processing in Fig. 15 can be implemented with low-speed electronic microcontrollers.

Carrier recovery is based on a phase-locked loop (PLL). The high-speed analog electronics stage is detailed in Fig. 16 for carrier recovery

based on optical PLL (OPLL) and electrical PLL (EPLL). In an OPLL (Fig. 16a), the LO laser is frequency-modulated by the frequency correction signal generated by the CR stage. Hence, an OPLL requires a LO laser with wideband frequency modulation (FM) response and short propagation delay in the LO path to minimize the overall loop delay. Minimizing the loop delay is one of the main challenges in OPLL design, since the loop includes the LO laser, 90° hybrid, photodiodes, and all the subsequent electronics in carrier recovery, which may not be realized within the same chip. Notably, Park et al. have demonstrated loop delays of only 120 ps for a highly integrated 40 Gbit/s binary PSK coherent receiver [53]. An EPLL (Fig. 16b) implementation eliminates requirements on LO laser FM response and on propagation delay at the cost of more complex analog electronics. Specifically, an EPLL requires a SSB mixer in each polarization to de-rotate the incoming signals (see Fig. 16b), since the transmitter and LO lasers are not phase locked. Additionally, the frequency offset between the transmitter and LO lasers must always be within the lock-in and hold-in ranges of the EPLL, which are practically limited by the voltage-controlled oscillator (VCO) frequency range (typically up to 10 GHz). This constraint can be satisfied by strict laser temperature control, whose cost and power consumption could be shared among several channels by using frequency combs for both the transmitter and LO. Alternatively, a frequency error estimation stage (Fig. 16b), based on a relatively simple frequency discriminator circuit [54], may be used to keep the LO laser frequency
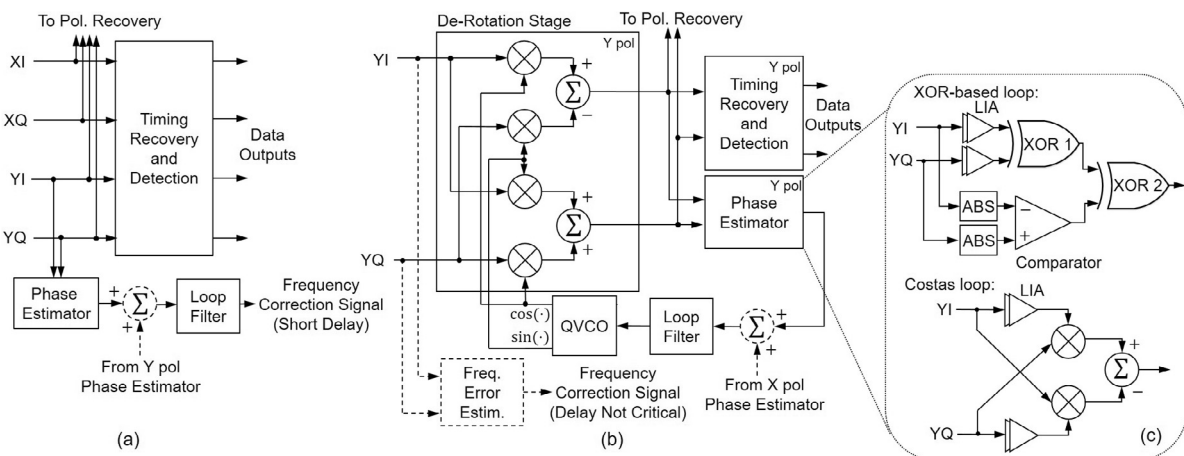

Fig. 16. Block diagrams of carrier recovery for an analog coherent receiver based on analog (a) OPLL and (b) EPLL (shown for one polarization only). The phase estimator block is detailed in (c), where LIA denotes limiting amplifiers, and ABS denotes full-wave rectifiers.
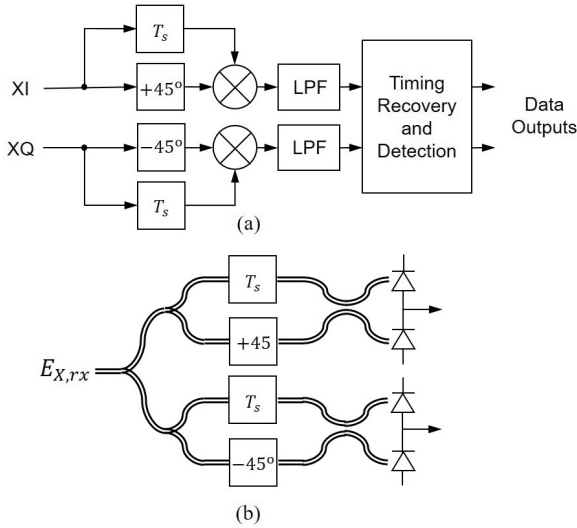
Fig. 17. Block diagrams of differentially coherent detection methods (a) with a local oscillator and (b) without a local oscillator. The inputs to the differentially coherent detection method in (a) are XI and XQ from Fig. 15. Optical delay interferometers are used for (b).

sufficiently close to the transmitter laser.

A PLL, either optical or electrical, consists of three basic stages: phase estimator, loop filter, and oscillator. The oscillator is the LO laser in an OPLL and an electronic VCO in an EPLL. The phase estimator stage wipes off the modulated data in order to estimate the phase error, which is then filtered by the loop filter, producing a control signal for the oscillator frequency. We consider a second-order loop filter [55] described by

$$F(s) = 2\xi\omega_n + \omega_n^2/s, \tag{24}$$

where ξ is the damping coefficient that is typically chosen to be $1/\sqrt{2}$ and ω_n is the loop natural frequency.

For both OPLLs and EPLLs, the phase estimator for the loop filter shown in Fig. 16b can be implemented using analog multipliers, as exemplified by the Costas loop phase estimator, or in a multiplier-free manner that simplifies receiver electronics, exemplified by the XOR-based phase estimator. Other multiplier-free phase estimator approaches have been proposed [55,56] to reduce receiver electrical complexity. The XOR-based phase estimator operates by estimating the sign of the phase error instead of its amplitude.

The receiver performance for either Costas or XOR-based loop depends on the phase error variance, which can be estimated using a small-signal approximation to linearize the PLL [12]:

$$\sigma_e^2 = \Delta\nu_{tot} \int_{-\infty}^{\infty} |j\omega + e^{-j\omega\tau_d}F(\omega)|^{-2}d\omega + 2(2\pi)^2k_F \int_{-\infty}^{\infty} |\omega|^{-1}|j\omega$$

$$+ e^{-j\omega\tau_d}F(\omega)|^{-2}d\omega + \frac{T_s}{2N_{PE}SNR}\frac{1}{2\pi}\int_{-\infty}^{\infty}\left|\frac{F(j\omega)}{j\omega + e^{-j\omega\tau_d}F(\omega)}\right|^2 d\omega, \tag{25}$$

where $\Delta\nu_{tot}$ is the sum of the transmitter laser and LO linewidths due to intrinsic phase noise, N_{PE} is the number of polarizations used to estimate phase error, k_F characterizes the magnitude of flicker noise [12], T_s is the symbol time and SNR is given by (21). The BER of a PSK signal with phase error distributed by $\mathcal{N}(0, \sigma_e^2)$ is then:

$$BER = Q(\sqrt{2SNR}) + \sum_{l=0}^{\infty} (-1)^l H_l\left(1 - \cos\left((2l+1)\frac{\pi}{4}\right)\exp\left(-\frac{(2l+1)^2\sigma_e^2}{2}\right)\right) \tag{26}$$

where σ_e^2 is given by (25) and

$$H_l = \frac{\sqrt{SNR}e^{-SNR/2}}{\sqrt{\pi}(2l+1)}\left(I_l\left(\frac{SNR}{2}\right) + I_{l+1}\left(\frac{SNR}{2}\right)\right) \geqslant 0, \tag{27}$$

where $I_l(x)$ is the modified Bessel function of the first kind. Note that the first term of (26) corresponds to error probability due to additive noise and is equivalent to (20) with $M = 4$. The second term accounts for the error caused by imperfect carrier phase recovery. Using Eqs. (25) (27), the BER of a PLL-based analog coherent receiver with a multiplier-free XOR phase detector can be estimated. The XOR phase detector shows minimal penalty relative to a traditional Costas loop, as well as minimal penalty using one polarization to estimate phase error versus two [12]. The Costas loop and XOR phase detector can be extended to 16-QAM by using the subset of constellation points on the diagonals to calculate phase error [56].

Fig. 14 shows the performance curves for an analog coherent receiver. At small dispersion, the penalty with respect to the DSP-based receiver is due to imperfect receiver filtering. In our simulations, the LPF is a fifth-order Bessel filter with bandwidth of 39.2 GHz ($0.7R_s$ for 224 Gbit/s DP-QPSK), for which $\Delta f = 40.7$ GHz. Hence, the imperfect receiver filtering results in a 1.6 dB penalty compared to DSP-based receiver. As dispersion increases, the receiver sensitivity decreases or OSNR required increases sharply, since the receiver does not equalize CD. Nonetheless, the sensitivity would allow unamplified eye-safe systems near 1310 nm to achieve a reach up to 40 km. In fact, systems with 100 GHz wavelength spacing could support 49 channels with 5 dB of margin, and systems with 200 GHz wavelength spacing could support 25 channels with 8 dB of margin.

7.3. Differentially coherent detection (DP-DQPSK)

Differentially coherent detection is performed by computing the phase difference between two consecutive symbols. This precludes the need of an absolute phase reference, and hence carrier phase recovery is not necessary. Differential detection, however, has some disadvantages compared to coherent detection. First, for the same spectral efficiency, differential detection has an inherent SNR penalty, e.g., ~ 2.4 dB for DQPSK compared to QPSK [25]. Second, differential detection restricts modulation to PSK formats.

Differential detection may be performed in the electrical domain or in the optical domain. Fig. 17a shows one implementation of differentially coherent detection, whereby the phase difference between two symbols is realized in the electrical domain. The XI and XQ signals in this figure correspond to the XI and XQ in Fig. 15, in which a LO laser is used to perform homodyne detection.

The polarization controller shown in Fig. 15 would only need two phase shifters, as the residual phase difference between the two polarizations that is compensated for by the third phase shifter is no longer needed, since the two polarizations are detected separately. One method to control the phase shifters is to minimize the radio frequency (RF) PSD of the optical signal after the final phase shifter. Minimization of this value ensures demultiplexing of the polarizations [57].

Since the receiver does not perform carrier recovery, the frequency difference between the LO and transmitter laser may be large. The BER of homodyne M-DPSK in the presence of frequency error is given by [58]:

$$BER = \frac{2}{\log_2 M}(F(\pi) - F(\pi/M))$$

$$F(\varphi) = \frac{\gamma_s\sin(\Delta\Psi - \varphi)}{4\pi}\int_{-\pi/2}^{\pi/2}\frac{\exp(-(\gamma_s - \gamma_s\cos(\Delta\Psi - \varphi)\cos t))}{\gamma_s - \gamma_s\cos(\Delta\Psi - \varphi)\cos t}dt, \tag{28}$$

where $\Delta\Psi = 2\pi f_{off}T_s$ is the phase error due to frequency offset f_{off} during a symbol period. As shown in [12], a 2-GHz frequency offset between transmitter and LO laser incurs nearly 3-dB SNR penalty. Fig. 14 shows the performance of homodyne DQPSK without frequency error. In unamplified systems, the LO laser provides sufficient gain that differential detection incurs only a small penalty relative to coherent detection. This penalty of differential detection relative to coherent

detection is also evident in amplified systems. Similar to a coherent receiver, an LO-based differentially coherent receiver detects the electric field; hence, DSP can be used for CD and PMD equalization. However, DSP-based differential detection is less appealing because carrier recovery necessary for coherent detection only accounts for 4.4% of the receiver power consumption.

The computation of the phase difference between two consecutive symbols may also be realized in the optical domain by using delay interferometers, as illustrated in Fig. 17b. The receiver electronics, in this case, must only perform timing recovery. This configuration does not employ a LO laser, which simplifies the receiver significantly. The delay caused by the delay interferometer is sensitive to the wavelength. As a result, the transmitter laser's frequency drifts can cause a penalty if not properly compensated by tuning the delay interferometer [59]. For DP-DQPSK, at 224 Gbit/s without delay interferometer tuning, a frequency drift of $\pm$ 800 MHz would incur a 2-dB penalty. The BER for a DQPSK signal can be calculated from (28) by setting $M = 4$ and $\Delta\Psi = 0$.

As shown by Fig. 14, DQPSK without an LO has significantly poorer receiver sensitivity in unamplified systems, such as intra-data center links. However, the OSNR required in amplified systems remains approximately the same as that of a LO-based DQPSK receiver. This makes LO-free DQPSK an attractive option for amplified inter-data center links that have optical CD compensation, as they have the lowest receiver complexity among coherent and differentially coherent receivers. Note that since the outputs of the balanced photodetection for differentially coherent detection without a LO laser are no longer linear in signal electric field values, CD and PMD cannot be equalized using DSP.

8. Complexity comparison

The previous sections compared the performance of the various modulation formats and detection techniques in terms of receiver sensitivity and OSNR required. This section focuses on the overall complexity and power consumption of these schemes.

Table 6 summarizes the main complexity differences between the various schemes discussed in this paper. This comparison covers the number of degrees of freedom (DOF), spectral efficiency, modulator type, complexity of the optical receiver, number of ADCs and their sampling rate and ENOB, capability to electronically compensate for CD, and DSP operations required at the receiver. The DD-compatible techniques have lower complexity, but they cannot scale beyond 100 Gbit/s due to their limited degrees of freedom and spectral efficiency. Stokes vector receivers offer intermediate optical complexity, while allowing up to three degrees of freedom and spectral efficiency up to 6 bits/s/Hz. Although the Stokes vector receiver provides improved

spectral efficiency, its performance (Fig. 11) in terms of receiver sensitivity or OSNR required is similar to that of DD-compatible formats such as 4-PAM. Moreover, its DSP complexity is comparable to that of DSP-based coherent optimized for short-reach applications, however without the same CD compensation capability.

Fig. 18 shows a coarse estimate of power consumption in 28-nm CMOS for various modulation schemes at 100 Gbit/s and 200 Gbit/s. The DSP-free receiver power consumption is estimated at 90-nm CMOS as detailed in [12]. The power consumption of DSP-based techniques is estimated using the power consumption models presented in [47]. First, the number of real additions and real multiplications is counted for all DSP operations (summarized in Table 6). Then, the power consumption is obtained by computing how much energy a given operation consumes. For instance, a real addition in 28-nm CMOS with 6-bit precision consumes 0.28 pJ, while a real multiplication with 6-bit precision consumes 1.66 pJ [47]. The power consumption estimates for DACs and ADCs assume that the power consumption scales linearly with resolution and sampling rate. The DAC figure of merit is 1.56 pJ/conv-step, while the ADC figure of merit is 2.5 pJ/conv-step [47]. The resolution of the DACs and ADCs, as well as the DSP arithmetic precision, is assumed equal to ENOB + 2, where ENOB is given in Table 6. Only OFDM formats are assumed to need high-resolution DACs, since single-carrier formats may avoid them assuming that pulse shaping and preemphasis are not performed. For all cases, the oversampling ratio assumed is $r_{os} = 5/4$, even though Stokes vector receivers and KK receivers have only been reported with $r_{os} = 2$.

Fig. 18(a and b) compare the power consumption of DD-compatible schemes at 100 Gbit/s for (a) a CD-compensated link where the residual CD is at most 80 ps/nm, and for (b) an 80-km uncompensated CD link. As expected, 4-PAM is more power efficient than the other formats. Compared to OFDM schemes, 4-PAM benefits from requiring lower sampling frequency, lower resolution, and performing time-domain equalization, which is more power efficient than frequency-domain equalization for short filters. However, in the high-uncompensated-CD regime, SSB modulation is the only viable choice. The SSBI cancellation in SSB-OFDM is assumed to be a Volterra nonlinear equalizer with 14 taps in (a) and 28 taps in (b). The power consumption of KK 4-PAM is excessively high due to the phase estimation using 3-times upsampling for computation of the Hilbert transform, as discussed in Section 5.3. Although not shown in Fig. 18, the power consumption of 4-PAM with MLSD in an uncompensated link would also be excessively high, since the complexity of the MLSD receiver grows exponentially with the memory length of the Viterbi decoder. We do not include MLSD 4-PAM in the comparison of Fig. 18 due to the lack of models to translate branch metric computations into power consumption.

Table 6
Complexity comparison. r_{os} denotes oversampling ratio, and $r_{CP} = \frac{N_{FFT} + N_{CP}}{N_{FFT}}$ is the oversampling ratio due to cyclic prefix in OFDM. Acronyms: Degrees of freedom (DOF), spectral efficiency (SE), optical hybrid (H), photodiode (PD), time-domain equalizer (TD-EQ), frequency-domain equalizer (FD-EQ), phase estimation (PE), single-input single output (SISO), carrier recovery (CR), and not applicable (NA).

| Scheme	DOF	SE (b/s/Hz)	Mod. type	Optical receiver	ADC (GS/bit)	# ADCs/ENOB	Digital CD comp.	DSP operations
4-PAM	1	2	IM	1 PD	$0.5r_{os}$	1/4	Very low	TD-EQ
16-QAM DC-OFDM	1	4	IM	1 PD	$0.5r_{os}r_{CP}$	1/5	Very low	IFFT/FFT, 1-tap FD-EQ
16-QAM SSB-OFDM	1	4	I&Q	1 PD	$0.5r_{os}r_{CP}$	1/5	Moderate	FD-EQ, SSBI cancellation
4-PAM KK	1	2	IM	1 PD	$0.5r_{os}$	1/5	Moderate	SSB filtering, KK-PE, and TD-EQ
Stokes 2-D: $2 \times$ 4-PAM	2	4	DP-IM	$2 \times 90°$ OH, 4 PD	$0.25r_{os}$	4/5	Very low	SISO and 3×1 MIMO
Stokes 3-D: $3 \times$ 4-PAM	3	6	DP-IM + PM	$90°$ OH, 4 PD	$0.16r_{os}$	4/5	Very low	4×3 MIMO
DSP-based DP-QPSK	4	4	DP I&Q	$2 \times 90°$ OH, LO, 4 PD	$0.25r_{os}$	4/4	High	EQ, 2×2 MIMO, CR
DSP-based DP-16-QAM	4	8	DP I&Q	$2 \times 90°$ OH, LO, 4 PD	$0.125r_{os}$	4/5	High	EQ, 2×2 MIMO, CR
DSP-free DP-QPSK	4	4	DP I&Q	$2 \times 90°$ OH, LO, 4 PD	NA	0	None	None
DSP-free DP-DQPSK	4	4	DP I&Q	$2 \times 90°$ OH, LO, 4 PD	NA	0	None	None
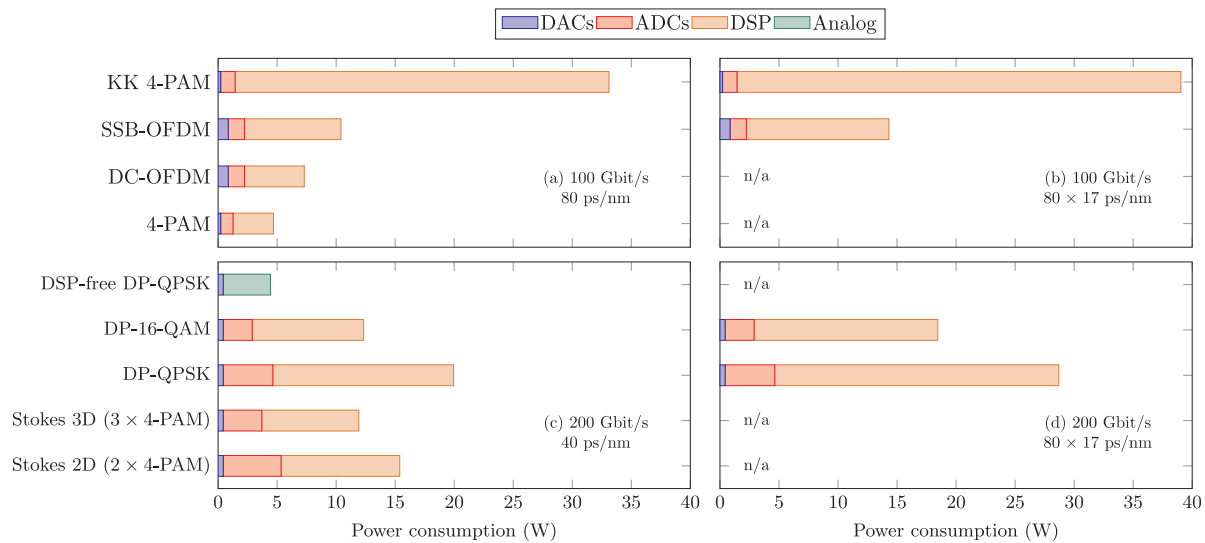
Fig. 18. Coarse estimate of power consumption of high-speed DACs, ADCs, and DSP for various modulation schemes at 100 Gbit/s and 200 Gbit/s. DSP power consumption estimates are made for 28-nm CMOS using the models presented in [47]. DSP-free receiver power consumption is estimated for 90-nm CMOS [12]. The graphs to the left assume that CD is compensated optically and the residual CD is at most 80 ps/nm at 100 Gbit/s (a) and 40 ps/nm at 200 Gbit/s (c). The graphs to the right assume uncompensated transmission up to 80 km near 1550 nm. In this regime, most techniques cannot work due to the high uncompensated CD.

Fig. 18(c and d) compare schemes with higher degrees of freedom at 200 Gbit/s for (c) a CD-compensated link where the residual CD is at most 40 ps/nm, and for (d) an 80-km uncompensated link. DSP-free coherent is more power efficient as it avoids high-speed ADCs and DSP, which comes at the expense of small tolerance to CD. In the small residual CD regime (Fig. 18c), DSP-based coherent receivers have similar power consumption to that of Stokes vector receiver. The LO laser in coherent receivers provides improved receiver sensitivity, and it may account for up to 2.5 W of the total receiver power consumption [47]. In the high-uncompensated-CD regime (Fig. 18d), DSP-based coherent is the only viable option. The results of Fig. 18(c and d) also illustrate that it is more power efficient to operate with higher constellation sizes and more degrees of freedom in order to minimize the symbol rate.

9. Conclusion

Increase in traffic within data centers, as well as between data centers, will demand higher per-wavelength bit rates. DD-compatible formats can meet these needs in the short-term, but more degrees of freedom are needed to support higher per-wavelength bit rates. Stokes vector receivers allow more degrees of freedom, but rely on power-hungry ADCs and DSP. Coherent and differentially coherent detection methods enable up to four degrees of freedom while significantly improving receiver sensitivity. However, conventional DSP-based coherent receivers designed for long-haul transmission, which prioritizes performance, are suboptimal for data center applications, which prioritize cost and power consumption. By reducing receiver complexity and making system performance tradeoffs, the power consumption of coherent links can be made low enough for intra- and inter-data center applications. Following this philosophy, LO-based DSP-free coherent receivers seem particularly promising for intra-data and inter-data center links, whereas amplified inter-data center links could also support LO-free differentially coherent receivers.

Funding

References

[1] Cisco, Cisco Global Cloud Index: Forecast and Methodology, 2015–2020, White Paper, 2016, pp. 1–41.

[2] M. Sharif, J.K. Perin, J.M. Kahn, Modulation schemes for single-laser 100 Gb/s links: single-carrier, J. Lightwave Technol. 33 (20) (2015) 4268–4277.

[3] J.K. Perin, M. Sharif, J.M. Kahn, Modulation schemes for single-wavelength 100 Gbit/s links: multicarrier, J. Lightwave Technol. (24) (2015) 5122–5132.

[4] J.L. Wei, J.D. Ingham, D.G. Cunningham, R.V. Penty, I.H. White, Comparisons between 28 Gb/s NRZ, PAM, CAP and optical OFDM systems for datacommunication applications, in: 2012 Optical Interconnects Conference, vol. 2, May 2012, pp. 3–4.

[5] K. Zhong, X. Zhou, T. Gui, L. Tao, Y. Gao, W. Chen, J. Man, L. Zeng, A.P.T. Lau, C. Lu, Experimental study of PAM-4, CAP-16, and DMT for 100 Gb/s short reach optical transmission systems, Opt. Express 23 (2) (2015) 1176–1189.

[6] M. Lauermann, R. Palmer, S. Koeber, P.C. Schindler, D. Korn, T. Wahlbrink, J. Bolten, M. Waldow, D.L. Elder, L.R. Dalton, J. Leuthold, W. Freude, C. Koos, Low-power silicon-organic hybrid (SOH) modulators for advanced modulation formats, Opt. Express 22 (24) (2014) 29927–29936.

[7] D. Patel, A. Samani, V. Veerasubramanian, S. Ghosh, D.V. Plant, Silicon photonic segmented modulator-based electro-optic DAC for 100 Gb/s PAM-4 generation, IEEE Photonics Technol. Lett. 27 (23) (2015) 2433–2436.

[8] J. Krause Perin, M. Sharif, J.M. Kahn, Sensitivity improvement in 100 Gbit/s-per-wavelength links using semiconductor optical amplifiers or avalanche photodiodes, J. Lightwave Technol. 34 (33) (2016) 5542–5553.

[9] S.H. Lee, A. Wonfor, R.V. Penty, I.H. White, G. Busico, R. Cush, M. Wale, Athermal colourless C-band optical transmitter for passive optical networks, in: European Conference on Optical Communication, ECOC, vol. 1–2, August 2015, 2010.

[10] T.N. Huynh, R. Watts, V. Vujicic, M.D.G. Pascual, C. Calo, K. Merghem, V. Panapakkam, F. Lelarge, A. Martinez, B.E. Benkelfat, A. Ramdane, L.P. Barry, 200-Gb/s Baudrate-Pilot-Aided QPSK/Direct detection with single-section quantum-well mode-locked laser, IEEE Photonics J. 8 (2) (2016).

[11] M. Chagnon, M. Morsy-Osman, D. Patel, V. Veerasubramanian, A. Samani, D. Plant, Digital signal processing for dual-polarization intensity and interpolarization phase modulation formats using stokes detection, J. Lightwave Technol. 34 (1) (2016) 188–195.

[12] J. Krause Perin, A. Shastri, J. Kahn, Design of low-power DSP-free coherent receivers for data center links, J. Lightwave Technol. 35 (21) (2017) 4650–4662.

[13] R. Urata, H. Liu, X. Zhou, A. Vahdat, Datacenter interconnect and networking: from evolution to holistic revolution, in: OFC, vol. W3G.1, 2017.

[14] M. Sumetsky, B. Eggleton, Fiber bragg gratings for dispersion compensation in optical communication systems, J. Opt. Fiber Commun. Rep. 2 (Sep 2005) 256–278.

[15] U. Troppenz, J. Kreissl, M. Möhrle, C. Bornholdt, W. Rehbein, B. Sartorius, I. Woods, M. Schell, 40 Gbit/s directly modulated lasers: physics and application, in: Proceedings of SPIE, vol. 7953, 2011, pp. 79530F–79530F–10.

[16] N.-N. Feng, D. Feng, S. Liao, X. Wang, P. Dong, H. Liang, C.-C. Kung, W. Qian, J. Fong, R. Shafiiha, Y. Luo, J. Cunningham, A.V. Krishnamoorthy, M. Asghari, 30 GHz Ge electro-absorption modulator integrated with 3 μm silicon-on-insulator waveguide, Opt. Express 19 (8) (2011) 7062–7067.

[17] C.R. Doerr, Silicon photonic integration in telecommunications, Front. Phys. 3 (August) (2015) 1–16.

[18] D. Thomson, A. Zilkie, J.E. Bowers, O. Alibart, V.D. Auria, M.D. Micheli, M. Smit, X. Leijtens, H. Ambrosius, E. Bente, An introduction to InP-based generic integration technology, Semicond. Sci. Technol. (2014) 1–41.

[19] G.-H. Duan, C. Jany, A.L. Liepvre, A. Accard, M. Lamponi, D. Make, P. Kaspar, G. Levaufre, N. Girard, J.-M. Fedeli, A. Descos, B.B. Bakir, S. Messaoudene, D. Bordel, S. Menezo, G.D. Valicourt, S. Keyvaninia, G. Roelkens, D.V. Thourhout, D.J. Thomson, F.Y. Gardes, G.T. Reed, Hybrid III – V on silicon lasers for photonic integrated circuits on silicon, IEEE J. Sel. Topics Quant. Electron. 20 (4) (2014).

[20] S. Koeber, R. Palmer, M. Lauermann, W. Heni, D.L. Elder, D. Korn, M. Woessner, L. Alloatti, S. Koenig, P.C. Schindler, H. Yu, W. Bogaerts, L.R. Dalton, W. Freude, J. Leuthold, C. Koos, Femtojoule electro-optic modulation using a silicon-organic hybrid device, Light: Sci. Appl. 4 (2) (2015) e255.

[21] A. Mercante, P. Yao, S. Shi, G. Schneider, J. Murakowski, D. Prather, 110 GHz CMOS compatible thin film LiNbO3 modulator on silicon, Opt. Express 24 (14) (2016) 15590–15595.

[22] C. Wang, M. Zhang, B. Stern, M. Lipson, M. Loncar, Nanophotonic lithium niobate electro-optic modulators, arXiv preprint arXiv:1701.06470, 2017.

[23] A. Shastri, C. Muzio, M. Webster, G. Jeans, P. Metz, S. Sunder, B. Chattin, Ultra-low-power single-polarization QAM-16 generation without DAC using a CMOS photonics based segmented modulator, J. Lightwave Technol. 33 (6) (2015) 1255–1260.

[24] A. Aimone, I.G. Lopez, S. Alreesh, P. Rito, T. Brast, V. Hohns, G. Fiolt, M. Grunert, DAC-free ultra-low-power dual-polarization 64-QAM Transmission with InP IQ Segmented MZM Module, in: OFC, 2016, p. Th5C.6.

[25] G.P. Agrawal, Fiber-Optic Communication Systems, Wiley, New York, 2002.

[26] J. McNicol, M. O'Sullivan, K. Roberts, A. Comeau, D. McGhan, L. Strawczynski, Electrical domain compensation of optical dispersion, in: OFC, vol. OThJ3, 2005.

[27] Q. Zhang, N. Stojanovic, X. Changsong, C. Prodaniuc, P. Laskowski, Transmission of single lane 128 Gbit/s PAM-4 signals over an 80 km SSMF link, enabled by DDMZM aided dispersion pre-compensation, Opt. Express 24 (21) (2016) 714–716.

[28] J. Lee, N. Kaneda, Y.K. Chen, 112-gbit/s intensity-modulated direct-detect vestigial-sideband pam4 transmission over an 80-km ssmf link, in: ECOC 2016; 42nd European Conference on Optical Communication, September 2016, pp. 1–3.

[29] D. Pilori, C. Fludger, R. Gaudino, Comparing DMT variants in medium-reach 100G optically amplified systems, J. Lightwave Technol. 34 (14) (2016) 3389–3399.

[30] H. Keangpo, J. Kahn, Multilevel optical signals optmized for systems having signal-dependent noises, finite transmitter extinction ratio and intersymbol interference, US Patent, 2 (12), 2004.

[31] K. Matsumoto, Y. Yoshida, A. Maruta, A. Kanno, N. Yamamoto, K.I. Kitayama, On the impact of tomlinson-harashima precoding in optical pam transmissions for intra-dcn communication, in: 2017 Optical Fiber Communications Conference and Exhibition (OFC), March 2017, pp. 1–3.

[32] R. Rath, D. Clausen, S. Ohlendorf, S. Pachnicke, W. Rosenkranz, Tomlinson-Harashima precoding for dispersion uncompensated PAM-4 transmission with direct-detection, J. Lightwave Technol. 35 (18) (2017) 3909–3917.

[33] C. Lenox, H. Nie, P. Yuan, G. Kinsey, A.L. Homles, B.G. Streetman, J.C. Campbell, Resonant-cavity InGaAs-InAlAs avalanche photodiodes with gain-bandwidth product of 290 GHz, IEEE Photonics Technol. Lett. 11 (9) (1999) 1162–1164.

[34] J. Armstrong, A.J. Lowery, Power efficient optical OFDM, Electron. Lett. 42 (6) (2006).

[35] J. Campello, Optimal discrete bit loading for multicarrier modulation systems, in: IEEE Symp. Info. Theory, Cambridge, MA, 1998, no. 1504, p. 193, 1998.

[36] W.A. Ling, Shaping quantization noise and clipping distortion in direct-detection discrete multitone, J. Lightwave Technol. 32 (2014) 1750–1758.

[37] K. Cho, D. Yoon, On the general BER expression of one- and two-dimensional amplitude modulations, IEEE Trans. Commun. 50 (2002) 1074–1080.

[38] S. Randel, D. Pilori, S. Chandrasekhar, G. Raybon, P. Winzer, 100-Gb/s discrete-multitone transmission over 80-km SSMF using single-sideband modulation with novel interference-cancellation scheme, in: European Conference on Optical Communication, ECOC, vol. 2015, no. 4, November, 2015.

[39] Z. Li, S. Erkilinc, K. Shi, E. Sillekens, L. Galdino, B. Thomsen, P. Bayvel, R. Killey, SSBI mitigation and Kramers-Kronig scheme in single-sideband direct-detection transmission with receiver-based electronic dispersion compensation, J. Lightwave Technol., no. to appear, 2017.

[40] L. Zhang, T. Zuo, Y. Mao, Q. Zhang, E. Zhou, G.N. Liu, X. Xu, Beyond 100-Gb/s transmission over 80-km SMF using direct-detection SSB-DMT at C-band, J. Lightwave Technol. 34 (2) (2016) 723–729.

[41] M.S. Antonio Mecozzi, Cristian Antonelli, Kramers-Kronig coherent receiver, Optica 3 (11) (2016) 1220–1227.

[42] C. Antonelli, M. Shtaif, A. Mecozzi, Kramers-Kronig PAM transceiver, in: OFC, 2017.

[43] M. Morsy-Osman, M. Chagnon, D.V. Plant, Four-dimensional modulation and stokes direct detection of polarization division multiplexed intensities, inter polarization phase and inter polarization differential phase, J. Lightwave Technol. 34 (7) (2016) 1585–1592.

[44] D.V. Plant, M. Morsy-Osman, M. Chagnon, Optical communication systems for datacenter networks, in: OFC, 2017.

[45] M. Morsy-Osman, M. Chagnon, M. Poulin, S. Lessard, D.V. Plant, 224-Gb/s 10-km transmission of PDM PAM-4 at 1.3 um using a single intensity-modulated laser and a direct-detection MIMO DSP-based receiver, J. Lightwave Technol. 33 (7) (2015) 1417–1424.

[46] M.Y.S. Sowailem, T.M. Hoang, M. Chagnon, M. Morsy-Osman, M. Qiu, S. Paquet, C. Paquet, I. Woods, O. Liboiron-Ladouceur, D. Plant, 100G and 200G single carrier transmission over 2880 and 320 km using an InP IQ modulator and Stokes vector receiver, Opt. Express 24 (26) (2016) 30485–30493.

[47] B.S.G. Pillai, B. Sedighi, K. Guan, N.P. Anthapadmanabhan, W. Shieh, K.J. Hinton, R.S. Tucker, End-to-end energy modeling and analysis of long-haul coherent transmission systems, J. Lightwave Technol. 32 (18) (2014) 3093–3111.

[48] C. Martins, F. Guiomar, S. Amado, R. Ferreira, S. Ziaie, A. Shahpari, A. Teixeira, A. Pinto, Distributive FIR-based chromatic dispersion equalization for coherent receivers, J. Lightwave Technol. PP (99) (2016) 5023–5032.

[49] J. Kahn, A. Gnauck, J. Veselka, S. Korotky, 4-Gb/s PSK Homodyne transmission system using phase-locked semiconductor lasers, IEEE Photonics Technol. Lett. 2 (4) (1990) 285–287.

[50] C.F. Liao, S.I. Liu, 40 Gb/s transimpedance-AGC amplifier and CDR circuit for broadband data receivers in 90 nm CMOS, IEEE J. Solid-State Circuits 43 (3) (2008) 642–655.

[51] R. Noe, H. Heidrich, D. Hoffmann, Endless polarization control systems for coherent optics, J. Lightwave Technol. 6 (Jul 1988) 1199–1208.

[52] H. Bulow, W. Baumert, H. Schmuck, F. Mohr, T. Schulz, F. Kuppers, W. Weiershausen, Measurement of the maximum speed of PMD fluctuation in installed field fiber, in: OFC/IOOC, 1999, pp. 83–85.

[53] H.-C. Park, M. Lu, E. Bloch, T. Reed, Z. Griffith, L. Johansson, 40 Gbit/s coherent optical receiver using a costas loop, Opt. Express 20 (26) (2012) 7.

[54] H.R. Rideout, J.S. Seregelyi, S. Paquet, J. Yao, Discriminator-aided optical phase-lock loop incorporating a frequency down-conversion module, IEEE Photonics Technol. Lett. 18 (22) (2006) 2344–2346.

[55] F. Gardner, Phaselock Techniques, Wiley, 2005.

[56] A. Mizutori, T. Abe, T. Kodama, M. Koga, Optical 16-QAM signal homodyne detection by extracting $+/-pi/4$ and $+/-3pi/4$-phase symbols, in: OFC, 2017, p. Th4C.6.

[57] C.R. Doerr, N.K. Fontaine, L.L. Buhl, PDM-DQPSK silicon receiver with integrated monitor and minimum number of controls, Photonics Technol. Lett., IEEE 24 (8) (2012) 697–699.

[58] R.F. Pawula, S.O. Rice, J.H. Roberts, Distribution of the phase angle between two vectors perturbed by Gaussian noise, IEEE Trans. Veh. Technol. 50 (2) (2001) 576–583.

[59] H. Kim, P.J. Winzer, Robustness to laser frequency offset in direct-detection DPSK and DQPSK systems, J. Lightwave Technol. 21 (9) (2003) 1887–1891.